

# **CONTROL STRATEGY FOR A PV-WIND BASED STANDALONE DC MICROGRID WITH HYBRID ENERGY STORAGE SYSTEM**

*A Project Report*

*submitted by*

**TONY THOMAS**

*in partial fulfilment of requirements*

*for the award of the degree of*

**MASTER OF TECHNOLOGY**



**DEPARTMENT OF ELECTRICAL ENGINEERING  
INDIAN INSTITUTE OF TECHNOLOGY MADRAS**

**MAY 2019**

# THESIS CERTIFICATE

This is to certify that the thesis titled **CONTROL STRATEGY FOR A PV-WIND BASED STANDALONE DC MICROGRID WITH HYBRID ENERGY STORAGE SYSTEM**, submitted by **TONY THOMAS**, to the Indian Institute of Technology, Madras, for the award of the degree of **Master of Technology**, is a bonafide record of the research work done by him under my supervision. The contents of this thesis, in full or in parts, have not been submitted to any other Institute or University for the award of any degree or diploma.

**Dr. Mahesh Kumar**  
Research Guide  
Professor  
Dept. of Electrical Engineering  
IIT-Madras, 600 036

Place: Chennai

Date:

## **ACKNOWLEDGEMENTS**

I would like to express my sincere and heartfelt gratitude to my project guide, Prof. Mahesh Kumar for his excellent guidance, motivation and constant support throughout the course of my project. His frequent interactions coupled with his patience have made this endeavour a success. I consider myself extremely fortunate to have had a chance to work under his supervision. I am also grateful for the laboratory facilities provided by him in the Power Quality and Automation Laboratory, ESB 354, Department of Electrical Engineering, which facilitated detailed simulation studies concerned to my work.

I greatly value and appreciate the encouragement by my fellow researchers and friends, who were always available as mentors and teachers in testing times. In this context I would like to extend my gratitude towards my fellow mates Jakeer Hussain, Srikanth Kotra, Durga Malleswara Rao, Satish R, N Pruthvi Chaitanya, Nafih Muhammad, Lokesh N and my entire M tech batchmates who spent their invaluable time to support every effort and achievement of mine.

I am also thankful to Director of Technical Education, Government of Kerala and AICTE for sponsoring me under QIP scheme.

In the end a special word of thanks to acknowledge the support of my wife Hrudya, my son Haron and my parents who always stood with me and were the source of inspiration for pursuing my endeavour. My heartfelt thanks to everyone who may have contributed to this endeavour, directly or indirectly.

Tony Thomas

# **ABSTRACT**

**KEYWORDS:** DC Microgrid; droop control; hybrid energy storage system; PMSG; power management strategy; PV.

This paper presents a control strategy for a PV-Wind based standalone DC Microgrid with a hybrid energy storage system. A control algorithm for power management has been developed for the better utilisation of renewable sources. The proposed system helps in reducing the voltage variation in the DC bus and the current stress in the battery due to intermittency of both solar and wind energy. The PV array and the wind system operating in MPPT are interfaced to the DC load using boost converters. The control algorithm during reduced power mode uses droop control strategy for keeping bus voltage constant under excess power condition. The controllers for battery and supercapacitor designed by frequency domain analysis are also presented. The system is tested for sudden change in load, renewable energies, reduced power mode and during load shedding using MATLAB-Simulink platform. The effectiveness of the proposed strategy is validated through simulation studies.

# TABLE OF CONTENTS

<b>ACKNOWLEDGEMENTS</b>	<b>i</b>
<b>ABSTRACT</b>	<b>ii</b>
<b>LIST OF TABLES</b>	<b>v</b>
<b>LIST OF FIGURES</b>	<b>vii</b>
<b>ABBREVIATIONS</b>	<b>viii</b>
<b>1 INTRODUCTION</b>	<b>1</b>
1.1 Motivation . . . . .	1
1.2 Literature Review . . . . .	2
1.3 Objective . . . . .	3
1.4 Scope of Work . . . . .	3
1.5 Overview and Structure of Work . . . . .	3
<b>2 SYSTEM ARCHITECTURE AND PHOTOVOLTAIC SYSTEM</b>	<b>5</b>
2.1 Architecture of DC Microgrid . . . . .	5
2.2 Photovoltaic System . . . . .	7
2.3 Equivalent Circuit of a PV Cell . . . . .	7
2.4 Boost Converter . . . . .	13
2.5 Summary . . . . .	14
<b>3 WIND ENERGY CONVERSION SYSTEM</b>	<b>15</b>
3.1 Structure of Wind Turbine . . . . .	15
3.2 System Setup . . . . .	18
3.3 MPPT Algorithms . . . . .	19
3.4 Wind Turbine Modeling . . . . .	20
3.5 Optimum Torque Control Strategy . . . . .	23
3.6 Permanent Magnet Synchronous Generator Modeling . . . . .	25

3.7	Summary . . . . .	26
<b>4</b>	<b>HYBRID ENERGY STORAGE CONTROL AND POWER MANAGEMENT STRATEGY</b>	<b>27</b>
4.1	Hybrid Energy Storage and Control . . . . .	28
4.2	Bidirectional DC DC Converters . . . . .	29
4.3	Design of PI Controller for HESS . . . . .	30
4.3.1	Supercapacitor Current Controller . . . . .	30
4.3.2	Battery Current Controller . . . . .	33
4.3.3	Voltage Controller . . . . .	36
4.4	State of Charge Estimation of Energy Storage System . . . . .	38
4.5	Power Management Strategy . . . . .	38
4.6	Reduced Power Mode . . . . .	39
4.7	Summary . . . . .	41
<b>5</b>	<b>SIMULATION RESULTS</b>	<b>42</b>
5.1	Case (i): When both Solar Irradiation and Wind Speed Varies . . . . .	42
5.2	Case (ii): When SoC of Battery Varies . . . . .	46
5.3	Case (iii): Pitch Angle Variation . . . . .	48
5.4	Case (iv): Change in Load Resistance . . . . .	48
5.5	Summary . . . . .	51
<b>6</b>	<b>CONCLUSION AND FUTURE SCOPE</b>	<b>52</b>
6.1	Conclusion . . . . .	52
6.2	Future Scope . . . . .	52
<b>A</b>	<b>POWERGUI BLOCK IN SIMULINK</b>	<b>53</b>

## LIST OF TABLES

2.1	Summary of P & O Algorithm . . . . .	11
5.1	System Parameters . . . . .	43

## LIST OF FIGURES

2.1	System architecture of DC microgrid . . . . .	6
2.2	Circuit schematic of DC microgrid . . . . .	6
2.3	PV cell, module and array [9] . . . . .	7
2.4	Single diode PV cell model . . . . .	8
2.5	P-V and I-V characteristics of PV array . . . . .	10
2.6	Perturb and observe algorithm for PV . . . . .	11
2.7	(a) Solar irradiance ( $W/m^2$ ) (b) PV output current (A) (c) temperature in °C (d) PV output power (watts) . . . . .	12
2.8	Boost converter . . . . .	13
3.1	Major components of a typical horizontal axis, three-bladed, upwind wind turbine [10] . . . . .	16
3.2	Typical power speed curve relationships in variable speed wind turbines . . . . .	19
3.3	$C_p$ versus tip speed ratio . . . . .	21
3.4	Mechanical output power versus turbine speed . . . . .	22
3.5	Optimum torque control of wind turbine system . . . . .	22
3.6	(a) Wind speed (m/s) (b) rotor speed (rad/s) (c) $C_p$ coefficient (d) wind output power (watts) . . . . .	24
3.7	(a) d-axis circuit (b) q-axis circuit . . . . .	25
4.1	The Ragone plot [13] . . . . .	27
4.2	Control system for hybrid energy storage . . . . .	28
4.3	Bidirectional converter with battery and supercapacitor . . . . .	29
4.4	Block diagram of supercapacitor controller . . . . .	30
4.5	Bode plot of compensated (Gidsc) and uncompensated (Gids) superca- pacitor current control loop. . . . .	33
4.6	Block diagram of battery current controller . . . . .	33
4.7	Bode plot of compensated (Gidc) and uncompensated (Gid) battery cur- rent control loop. . . . .	36



4.8	Bode plot for compensated ( $G_{vidc}$ ) and uncompensated ( $G_{vid}$ ) DC link voltage control loop. . . . .	37
4.9	Flowchart for power management . . . . .	39
4.10	Droop control scheme in reduced power mode . . . . .	41
5.1	Performance under case (i): (a) Solar irradiance ( $W/m^2$ ) (b) wind speed (m/s) (c) $P_L$ -load power, $P_{pv}$ -PV power, $P_w$ -wind power, $P_{ESS}$ -energy storage system power (W) (d) battery current (A) (e) DC link voltage (V) . . . . .	44
5.2	Performance under case (i): (a) SoC of battery (b) SoC of supercapacitor . . . . .	45
5.3	Performance under case (i): (a) Tip speed ratio (b) $C_p$ coefficient . . . . .	45
5.4	Performance under case (ii), variation of SoC of battery: (a) SoC of battery (b) SoC of supercapacitor (c) DC link voltage (V) (d) load current (A) . . . . .	46
5.5	Performance under case (ii), variation of SoC of battery: (a) PV power (W) (b) wind power (W) (c) energy storage system power (W) (d) load power (W) (e) battery current (A) (f) supercapacitor current (A) . . . . .	47
5.6	Case (iii): (a) $P_L$ -load power, $P_{PV}$ -PV power, $P_W$ -wind power, $P_{ESS}$ -energy storage system power (W) (b) DC link voltage (V) (c) $v_w$ - wind speed (m/s), $\beta$ - pitch angle (deg) . . . . .	49
5.7	Case (iv): (a) $P_L$ -load power, $P_{PV}$ -PV power, $P_W$ -wind power, $P_{ESS}$ -energy storage system power (W) (b) load current (A) (c) DC link voltage (V) (d) battery current (A) . . . . .	50
5.8	Case (iv): SoC of supercapacitor . . . . .	51

## **ABBREVIATIONS**

<b>PV</b>	Photo Voltaic
<b>PMSG</b>	Permanent Magnet Synchronous Generator
<b>ESS</b>	Energy Storage Systems
<b>MPPT</b>	Maximum Power Point Tracking
<b>MPP</b>	Maximum Power Point
<b>P &amp; O</b>	Perturb and Observe
<b>WECS</b>	Wind Energy Conversion System
<b>HAWT</b>	Horizontal Axis Wind Turbine
<b>FSWT</b>	Fixed Speed Wind Turbine
<b>VWST</b>	Variable Speed Wind Turbine
<b>HCS</b>	Hill Climb Search Algorithm

# CHAPTER 1

## INTRODUCTION

A microgrid is defined as a group of Distributed Energy Resources (DERs), including Renewable Energy Resources (RES) and Energy Storage Systems (ESS) and loads, that operate together locally as a single controllable entity [1]. Microgrids exist in various sizes and configurations; they can be large and complex networks with various generation resources and storage units serving multiple loads, or small and simple systems supplying a single customer. Microgrids exist in both grid connected and islanded forms. Grid connected microgrids have a Point of Interconnection (POI) or Point of Common Coupling (PCC) with a large power network. In both grid connected and islanded/isolated operation modes, microgrids should maintain balance between generation and consumption, while satisfying reliability, power quality and adequate standards. Isolated microgrids have no POI or PCC. The vertically integrated bulk power system has now been changed to a smart decentralised network with the growth of microgrid.

### 1.1 Motivation

The most promising methodology for remote electrification and/or decrease in dependence on fossil fuel based energy source is the idea of renewable based hybrid electric system. The use of fossil fuels leads to  $CO_2$  emission and environmental pollution. So by the use of clean energy resources, greenhouse gas emission can be reduced. The solar and wind are the most abundant renewable sources available in nature. The hybrid combination of solar and wind energy can provide continuous power to load than an individual source alone. The solar and wind sources are intermittent, uncontrollable, stochastic and highly variable, their integration in the electric power grid poses challenges to its effective operation. Innovative technologies and novel control algorithms are required to alleviate various problems such as load mismatch, poor load following, voltage instability, inferior power quality and reliability problems, to increase the penetration of RE sources in the electric power grid.

## 1.2 Literature Review

The photovoltaic energy is one of the renewable energies that has been attracted by researchers all over the world. The conversion efficiency of PV arrays are very low, it requires maximum power point control algorithms to harness maximum energy. The direct and indirect methods for MPPT algorithms are described in [2]. The use of wind energy to meet the energy demand has a great advancement over the past decades. The various methods used for obtaining maximum output power from wind energy system has been studied in [3]. A comparison has been made in this paper among various MPP methods in terms of convergence time, efficiency, training, complexity and wind measurement. The use of supercapacitor along with battery improves and enhances the life of battery [4]. The batteries have low power density and limited charge/discharge cycles. The supercapacitors are high-power storage devices which are mainly used to smooth the peak power applied to the battery and to deliver full power during short grid outages. A supercapacitor is a double-layer electrochemical capacitor that can store thousand times more energy than a typical capacitor. It shares the characteristics of both batteries and conventional capacitors. Moreover, they have almost negligible losses and long lifespan. They can process a large number of charge and discharge cycles (several hundred thousand cycles) compared to only a few thousand cycles for lead-acid batteries and can supply much higher currents than batteries. An energy management system for a laboratory scale microgrid based on wind-PV-battery is proposed in [5]. The control algorithm developed in this provides stable operation of the system under various power generation and load conditions. A DC link voltage controller with PV-battery-supercapacitor combination based grid interactive supervisory power management system is proposed in [6]. The power management system proposed in this considers renewable power variation, grid availability, electricity pricing and changes in local loads. A DC Microgrid with a decentralised droop control with multiple distributed renewable energy sources and constant power load is studied in [7]. This paper considers voltage and power fluctuations control due to source disturbances and load change.

## **1.3 Objective**

The objective of the thesis is the proposal of a control strategy for a DC microgrid containing hybrid renewable sources with a hybrid storage system. It can be summarised as follows:

- 1) The integration of solar and wind energy with battery and supercapacitor to provide reliable, adequate power to meet load demand.
- 2) A power management strategy for better control and management of power.
- 3) The proposed system should reduce voltage variation in the DC bus and the current stress in the battery due to the intermittency of both solar and wind energy.
- 4) The design of battery and supercapacitor by frequency domain analysis to meet the steady state and transient requirements when both wind and PV changes simultaneously.
- 5) The load requirement should be shared between PV and wind when battery is fully charged and the system is operating in excess power condition by means of droop control.
- 6) The reduction of wind power during high wind speeds by varying the pitch angle.

## **1.4 Scope of Work**

The work find applications in rural/remote areas where grid interconnection and maintenance is a techno-economic challenge. The use of abundant renewable sources, solar and wind can make a country to meet ever increasing energy demand. The use of solar and wind is eco friendly and reduces environmental pollution.

## **1.5 Overview and Structure of Work**

Chapter 2 deals with the architecture of DC microgrid and the photovoltaic systems. The equivalent circuit of a PV cell, the perturb and observe algorithm for maximum power point tracking are described in this section.

Chapter 3 explains the system set up for wind energy conversion. The structure of wind turbine, the modeling of wind turbine and optimum torque based control strategy are

outlined in this chapter.

Chapter 4 narrates hybrid energy storage system and its control strategy. The chapter also explains the power management algorithm for power balancing between distributed sources and load. The droop controller for reduced power mode for sharing the load between solar and wind is also described.

Chapter 5 shows the performance of the integrated system by simulating using MATLAB-Simulink platform. The system is tested for different cases and the results are discussed in this chapter.

Chapter 6 concludes the work along with a discussion for future scope.

## CHAPTER 2

# SYSTEM ARCHITECTURE AND PHOTOVOLTAIC SYSTEM

Microgrids can be of AC or DC type to deliver power, but DC microgrid is favoured due to the reduction in complexity of control, absence of grid synchronization issues, harmonics, reactive power and reduction in conversion losses due to inverter [8]. In many of the countries, the household, domestic, data and telecom centres, mobile towers are electrified by DC grids. The autonomous or isolated DC microgrid also find applications in electric vehicles, naval ships, spacecraft and submarines. Storage devices are also used along with renewables to provide efficient, good quality, reliable and optimum power. A hybrid combination of renewables with hybrid storage devices can provide a good power management between source and load.

### 2.1 Architecture of DC Microgrid

The DC microgrid considered in this work is illustrated in Fig. 2.1. The system consists of the PV array, Permanent Magnet Synchronous Generator (PMSG) based wind turbine system, battery, supercapacitor and power electronic converters. The DC loads connected to the DC bus are of resistive type. Battery and supercapacitor are connected to the DC grid using two bidirectional DC-DC converters. The circuit schematic of the architecture is given in Fig. 2.2. Here the hybrid energy storage system regulates the DC bus voltage and also manages the power flow between distributed energy resources and load. The capacitor,  $C_{dc}$  is the DC link. When the PV and wind power generation are less than the load demand, the DC bus voltage decreases. To address the power deficiency, the energy storage systems (ESS) provides the surplus power demand. Analogously, when the PV and wind generation are more than the load demand, the energy storage systems will absorb the surplus power generation. When the battery discharges to the lower limit, load is cut out to maintain power balance. When battery reaches upper limit, the PV and wind system operates at off-MPPT mode. In the whole

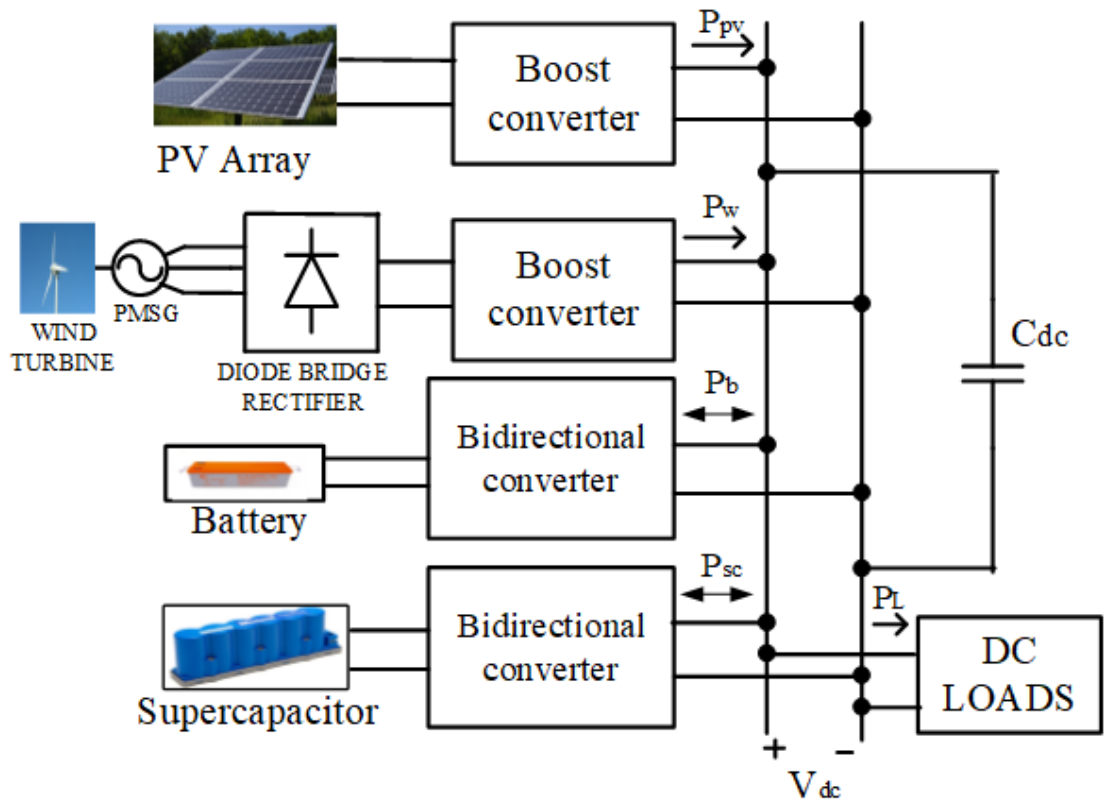


Figure 2.1: System architecture of DC microgrid

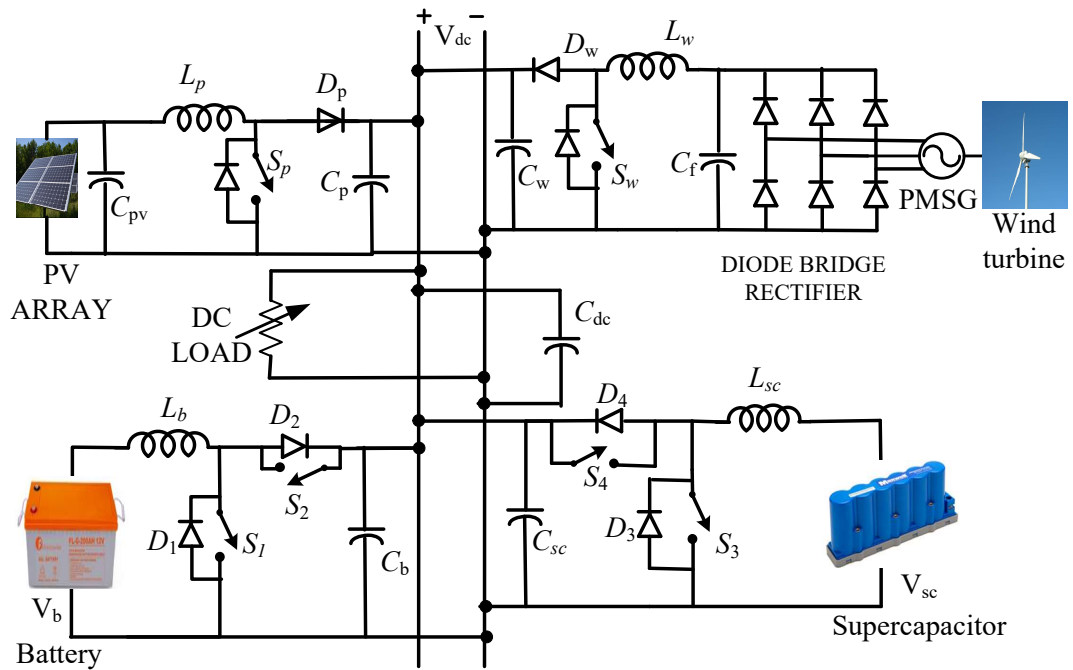


Figure 2.2: Circuit schematic of DC microgrid



process, the supercapacitor provides the oscillating and the transient power, based on its SoC condition.

## 2.2 Photovoltaic System

A solar or a photovoltaic cell converts solar energy to electrical energy by photovoltaic effect. A solar cell produces current when sunlight is irradiated on it. The electron-hole pairs are generated when PV cell materials absorb photons having energy exceeding the band-gap of the material. These generated carriers are swept apart by the internal electric fields of this cell and they contribute to current when the cell is connected to the external circuit. A number of PV modules are arranged in series and parallel to meet the energy requirements. The output power of a PV system depends upon solar irradiation, atmospheric temperature, area and efficiency of the PV array. A PV array consists of several photovoltaic modules in series and parallel as shown in Fig. 2.3.

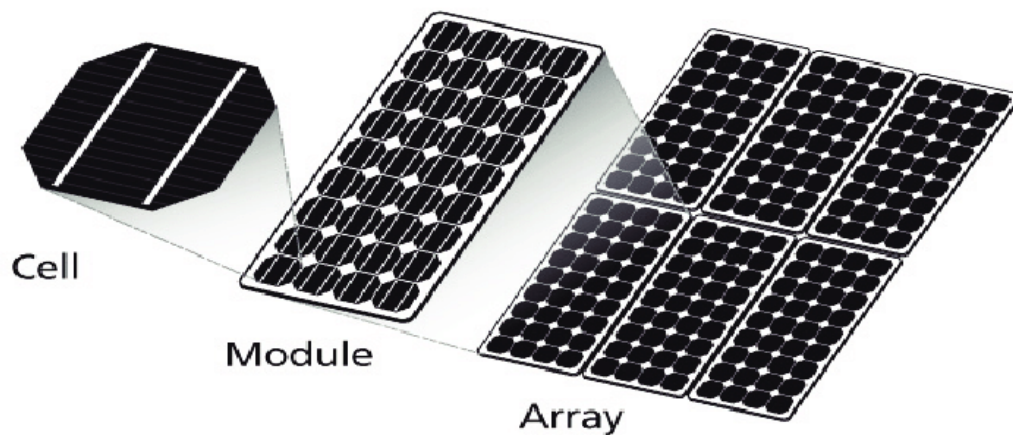


Figure 2.3: PV cell, module and array [9]

Series connection of modules increases the voltage and parallel connection increases the current in the array.

## 2.3 Equivalent Circuit of a PV Cell

An ideal solar cell is represented by a current source in parallel with a diode. The single diode model of a PV cell is shown in Fig. 2.4. When the cell is exposed to light,

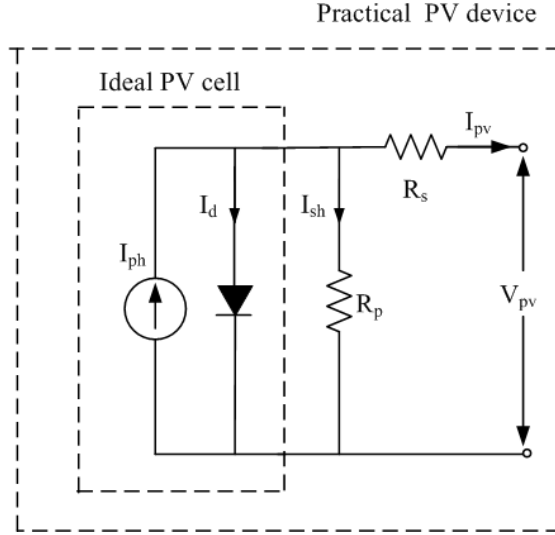


Figure 2.4: Single diode PV cell model

direct current is generated that varies linearly with solar radiation. The model can be represented by including a series resistance ( $R_s$ ) and a shunt resistance ( $R_p$ ). Here,  $R_s$  is introduced for considering the voltage drops and internal losses (contact resistance, resistance of p and n bodies) due to flow of current and  $R_p$  takes into account the leakage current of pn junction and depends on the fabrication method of PV cell.

The fundamental equations for a PV cell can be modelled from the theory of Shockley diode equation and semiconductor theory. An ideal PV cell can be mathematically represented as

$$I_{pv} = I_{ph} - I_d \quad (2.1)$$

where  $I_{pv}$  is the output PV current,  $I_{ph}$  is the current generated by the incident light,  $I_d$  is the Shockley diode equation. The diode current  $I_d$  is given by Shockley diode equation,

$$I_d = I_0(e^{u'} - 1) \quad (2.2)$$

where

$$u' = \frac{V_{pv}q}{AkT} \quad (2.3)$$

A is ideality factor, its value is 1.6,  $V_{pv}$  is the output voltage of PV module, k is the Boltzmann constant ( $1.3806 \times 10^{-23}$  J/K), q is the electron charge ( $1.6 \times 10^{-19}$  C).

The practical PV modules are composed of several connected PV cells. The single

diode model of a practical PV device can be represented as

$$I_{pv} = I_{ph} - I_d - I_{sh} \quad (2.4)$$

The diode current  $I_d$  is given by

$$I_d = I_0(e^u - 1) \quad (2.5)$$

where

$$u = \frac{(I_{pv}R_s + V_{pv})q}{AkTN_s} \quad (2.6)$$

$N_s$  is the number of cells connected in series,  $I_{ph}$  is the photovoltaic current of the PV module. The term  $kTN_s/q$  can be defined as voltage equivalent of temperature of the module as  $V_T$ . The cells connected in series provide greater output voltage. The term  $I_{pv}R_s + V_{pv}$  is the voltage across the diode.

The photo current, current generated by the incident light ( $I_{ph}$ ) depends linearly on the solar irradiation and is also influenced by the temperature according to the following equation:

$$I_{ph} = \frac{G_{irradiance}}{G_{irradianceSTC}} [k_i (T - T_{ref}) + I_{scref}] \quad (2.7)$$

$T_{ref}$  is the reference temperature,  $T$  is the module operating temperature,  $I_{scref}$  is the cell's short circuit current at standard conditions (298 K and 1000 W/m<sup>2</sup>),  $k_i$  is the short circuit current temperature coefficient,  $G_{irradianceSTC}$  is the reference solar irradiance (1000 W/m<sup>2</sup>),  $G_{irradiance}$  is the irradiation on the solar surface.

The reverse saturation or leakage current of diode  $I_0$  is given by

$$I_0 = I_{rs} \left( \frac{T}{T_{ref}} \right)^3 e^{\frac{qE_{go}}{Ak} \left( \frac{1}{T} - \frac{1}{T_{ref}} \right)} \quad (2.8)$$

where

$$I_{rs} = \frac{I_{scref}}{\left( e^{\frac{qV_{oc}}{kTAN_s}} - 1 \right)} \quad (2.9)$$

$E_{go}$  is the material band gap energy (1.12 eV for polycrystalline Silicon),  $V_{oc}$  is open circuit voltage.

If the PV array is composed of  $N_p$  number of modules connected in parallel, output

current of PV array ( $I_{pv}$ ) is given by

$$I_{pv} = N_p [I_{ph} - I_0(e^u - 1)] - \frac{V_{pv} + I_{pv}R_s}{R_p} \quad (2.10)$$

In (2.10)  $R_p$  is usually very high, so the term  $\frac{V_{pv} + I_{pv}R_s}{R_p}$  can also be neglected.

The designed photovoltaic system consists of 7 series modules and 4 parallel modules. Its output is connected to DC bus through a DC-DC boost converter. The P-V characteristics and I-V characteristics of the PV array is shown in Fig. 2.5. The Maxi-

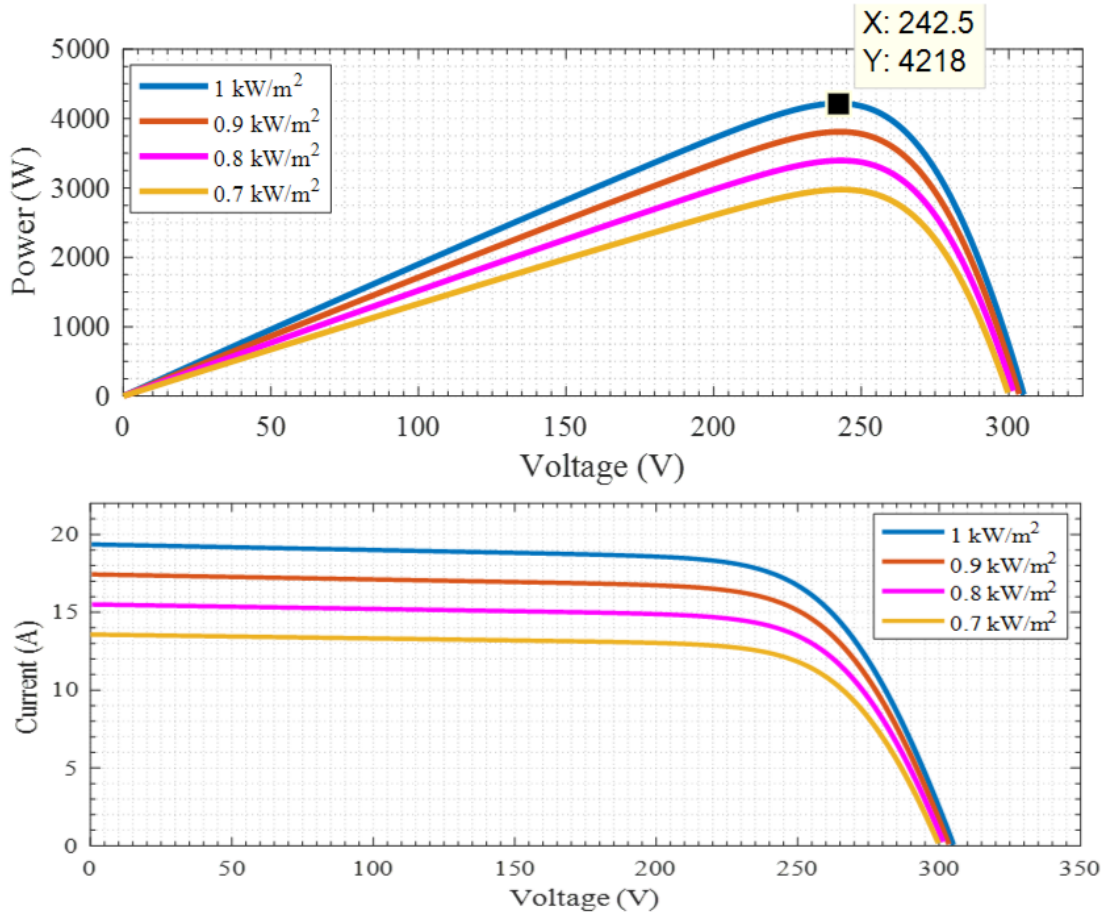


Figure 2.5: P-V and I-V characteristics of PV array

imum Power Point Tracking (MPPT) method used is Perturb and Observe algorithm. It is also known as Hill climbing algorithm. In this algorithm when the operating voltage of the PV panel is perturbed by a small increment, if the resulting change in power  $P$  is positive, then we are going in the direction of maximum power point (MPP) and we keep on perturbing in the same direction. If  $P$  is negative, we are going away from the direction of MPP and the sign of perturbation supplied has to be changed. The summary

of P and O algorithm is shown in Table 2.1.

Table 2.1: Summary of P & O Algorithm

Perturbation	Change in power	Next Perturbation
Positive	Positive	Positive
Positive	Negative	Negative
Negative	Positive	Negative
Negative	Negative	Positive

The process is repeated until MPP is reached. There the operating point oscillates around the MPP. The flowchart of MPPT is shown in Fig. 2.6. The duty ratio gener-

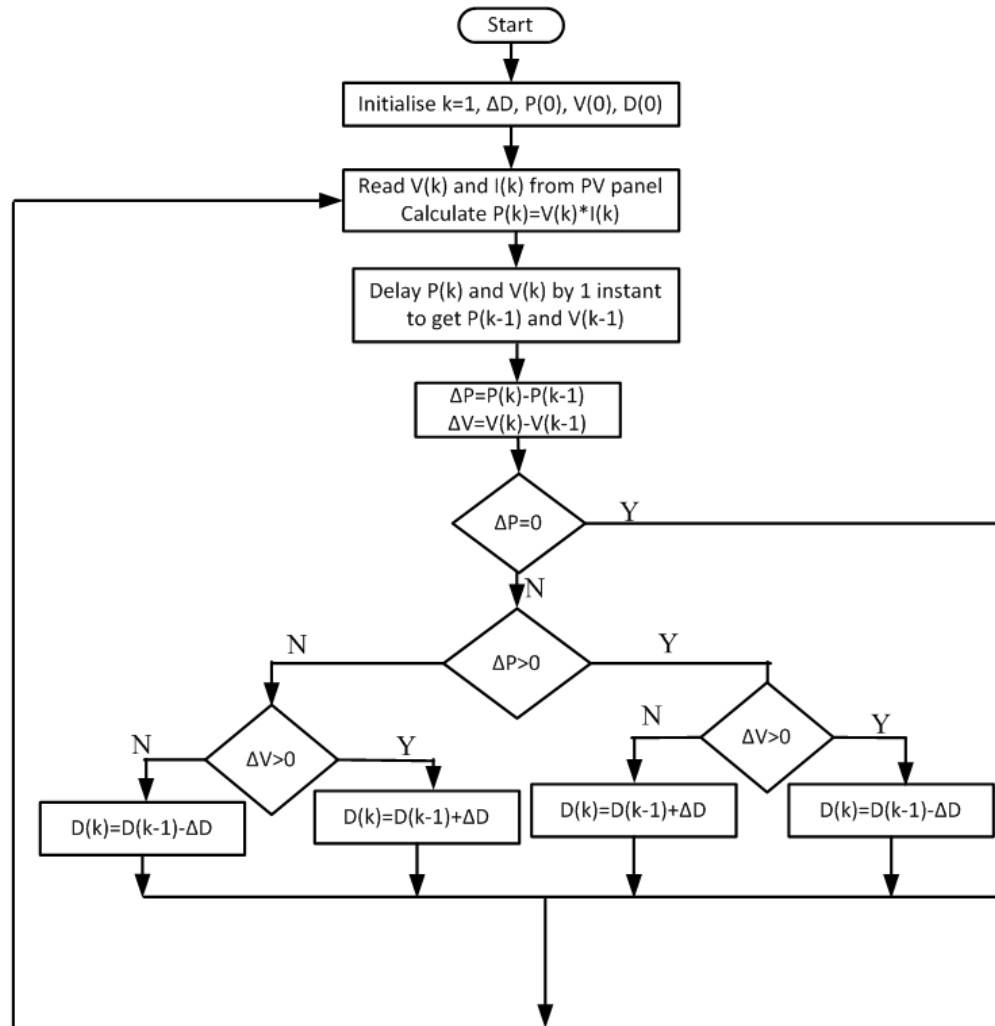


Figure 2.6: Perturb and observe algorithm for PV

ated by the MPPT control block is given to the boost converter. The perturbation size and time interval between iterations should be considered to achieve faster tracking of maximum power point. The variation of PV power with solar irradiance during MPPT

operation is plotted in Fig. 2.7. The PV output power obtained for irradiances (600,

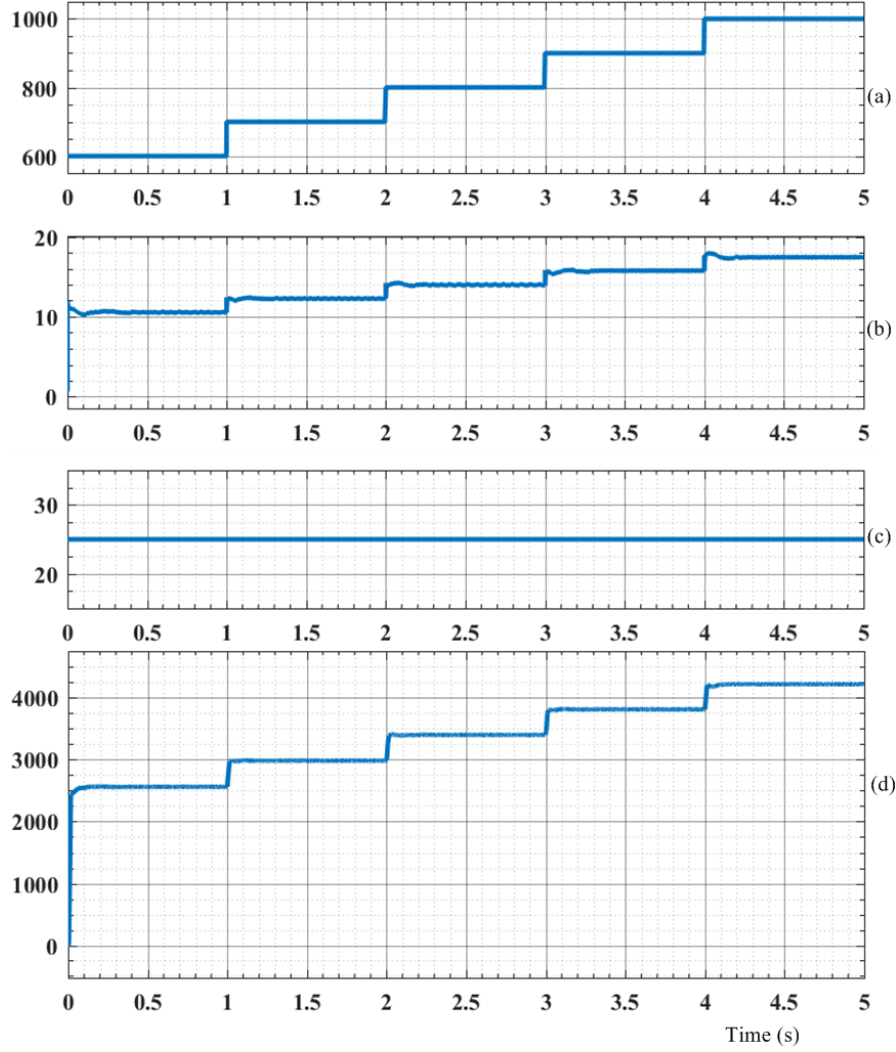


Figure 2.7: (a) Solar irradiance ( $W/m^2$ ) (b) PV output current (A) (c) temperature in  $^{\circ}C$  (d) PV output power (watts)

700, 800, 900, 1000)  $W/m^2$  are (2553, 2977, 3395, 3808, 4218) watts respectively. The main advantage of P & O method is that it is easy to implement, it is very generic, it has low computational demand and it does not require any information about PV array, but needed only the measured voltage and current. The main disadvantages of P & O are the oscillations around the MPP in steady state conditions, and poor tracking under rapidly changing irradiances. Variable step size and variable perturbation frequency based improved P & O algorithms are available for better dynamic performance.

## 2.4 Boost Converter

The boost topology is used for stepping up the low voltage input from the PV. The boost converter consists of a dc input voltage  $V_{in}$ , inductor  $L_p$ , controlled switch S1, diode D1 and filter capacitor  $C_p$ . When S1 is ON, current in the inductor increases linearly and the diode D1 will be in OFF state. When the switch S1 is turned off, the energy stored in the inductor is released through D1 to output load through  $C_p$ . The circuit diagram of boost converter is shown in Fig. 2.8. The boost converter can operate in

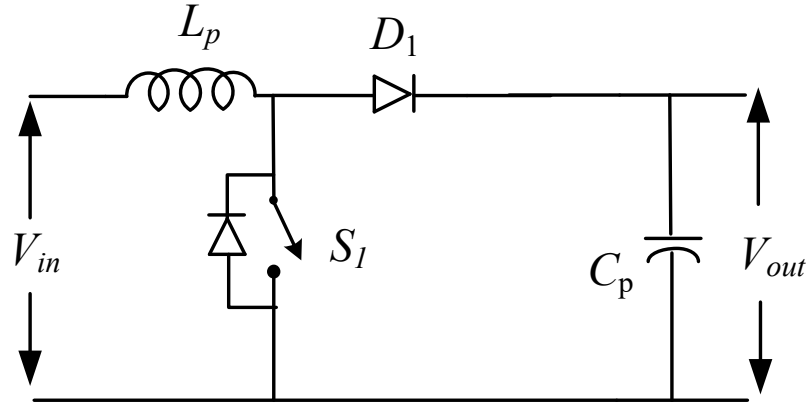


Figure 2.8: Boost converter

continuous conduction mode or in discontinuous conduction mode. The output voltage  $V_{out}$  is given by

$$\frac{V_{out}}{V_{in}} = \frac{1}{1 - D} \quad (2.11)$$

where  $V_{in}$  is the input voltage,  $V_{out}$  is the output voltage and D is the duty cycle.

$V_{out} = 400$  V;  $V_{in} = 242.2$  V;

the value of D = 0.3948;

Using small signal analysis

$$\frac{\Delta i_L}{I_L} = \frac{(1 - D)^2 D T_s}{\frac{L}{R}} \quad (2.12)$$

Assuming 1 % ripple in inductor current,

$$0.01 = \frac{(1 - 0.3948)^2 * 0.3948 * 20}{L_p * 15 * 10^3} \quad (2.13)$$

$$L_p = 19.28 \text{ mH}$$

Filter capacitor is used at output to limit the output voltage ripple. The filter capacitor provides current to the load when the diode D1 is off. The minimum value of filter capacitance required at output for having voltage ripple less than 1% is given by

$$\frac{\Delta v_{out}}{V_{out}} = \frac{D}{fRC} \quad (2.14)$$

$$C_p = \frac{D * V_{out}}{\Delta v_{out} * R * f} \quad (2.15)$$

$$0.01 = \frac{0.3948}{15 * 10^3 * 20 * C_p} \quad (2.16)$$

$$C_p = 131 \mu\text{F}$$

## 2.5 Summary

The architecture of the DC microgrid and the photovoltaic system are described in this chapter. The modeling of PV cell, the perturb and observe algorithm for maximum power extraction are also explained. The MPPT algorithm for different solar irradiations are verified with the PV output power.



## **CHAPTER 3**

### **WIND ENERGY CONVERSION SYSTEM**

Wind is commercially and operationally the most viable renewable energy resource and accordingly, emerging as one of the largest source in the renewable energy sector. The wind power generation possesses advantages over conventional power project such as fuel cost is zero, construction time is less, operation and maintenance cost is low, capacity addition can be in modular form and no adverse effect on global environment. Wind Energy Conversion Systems (WECS) are cheaper than photovoltaic energy conversion systems of the same power rating.

#### **3.1 Structure of Wind Turbine**

A wind energy conversion system consists of a turbine tower which carries the nacelle, and a wind turbine rotor which consists of rotor blades and hub. Most modern wind turbines are horizontal-axis wind turbines (HAWTs) with three rotor blades usually placed upwind of the tower and the nacelle, as illustrated in Fig. 3.1. On the outside, the nacelle is usually equipped with anemometers and a wind vane to measure the wind speed and direction, as well as with aviation lights. The nacelle contains the major components of wind turbine, i.e. the gearbox, mechanical brake, electrical generator, control systems, yaw drive, etc. The major parts are described below.

##### **1) Tower**

The wind turbines are mounted on the tower. The wind turbines mounting on the highest possible tower results in increased power production due to the stronger winds present at higher altitudes. But there are some limitations as how much height of a tower is appropriate for a given application. One such consideration is the structural requirement necessary to support the turbine being considered, including how much the turbine weighs as well as what types of environmental forces (high winds, snow, rain) it will have to sustain over time.

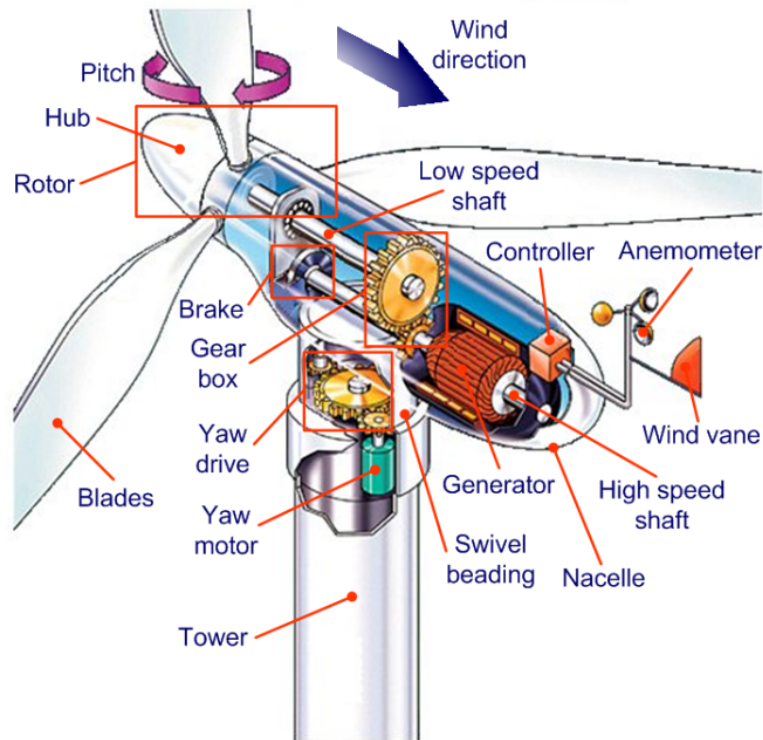


Figure 3.1: Major components of a typical horizontal axis, three-bladed, upwind wind turbine [10]

## 2) Rotor

The rotor is the heart of a wind turbine and consists of multiple rotor blades attached to a hub. It is the turbine component responsible for collecting the energy present in the wind and transforming this energy into mechanical motion. Turbines are often designed around a certain diameter rotor. The predominant aerodynamic principles that rotor is designed are based upon are Drag Design and Lift Design. Drag design rotors operate on the idea of the wind pushing the blades out of the way, thereby setting the rotor into motion. With lift design rotors, the blades are designed to function like the wing of an airplane. Each blade is designed as an air foil, creating lift as the wind moves past the blades. The air foil operates on the basis of Bernoulli's principle where the shape of the blade causes a pressure differential between its upper and lower surfaces. This difference in pressure causes an upward force that lifts the air foil. In this case, this lift causes the rotor to rotate for transforming the energy in the wind into mechanical motion.

## 3) Hub

The hub is the centre of the rotor to which the rotor blades are attached. Cast iron

or cast steel is most often used. The hub directs the energy from the rotor blades on to the generator. If the wind turbines have a gearbox, the hub is connected to the slowly rotating gearbox shaft, converting the energy from the wind into rotation energy. If the turbine has a direct drive, the hub passes the energy directly on to the generator.

#### **4) Power control of wind turbine**

Wind turbines are generally designed to yield maximum power (nominal capacity) at rated (or nominal) wind speed. In case of stronger winds it is necessary to waste part of the excess energy of the wind to avoid damages to the wind turbine. Pitch angle control was developed by turning the rotor blades into or out of the wind according to the control laws. An anemometer mounted atop the nacelle constantly checks the wind speed and sends signals to the pitch actuator, adjusting the angle of the blades to capture the energy from the wind most efficiently. Standard modern turbines usually pitch the blades at high winds in order to prevent the rotational speed from rising to an unacceptably dangerous level. A slewing drive precisely angles the blade for pitch control.

#### **5) Nacelle**

The nacelle contains all the machinery of the wind turbine, i.e. the drive train including the mechanical transmission (rotor shaft, bearings and the gearbox), the electrical generator, and other equipments such as the power electronic interface, the yaw drive, the mechanical brake and the control system. Because it requires rotating in order to track the wind direction, it is connected to the tower via bearings. The generator converts the mechanical motion of the rotor into electrical energy. The power electronic converters are used by wind turbines as an interface between the load/generator and the grid. The power electronic converter enables wind turbines to operate at variable speed, and thus allows to provide more effective power capture than the fixed-speed type. The wind turbine contains two types of brakes, blade tip brake and mechanical brake. The mechanical drum brake or disk brake is used only as an emergency brake, if the blade tip brake fails.

#### **6) Yaw drive**

The yaw drive is an important component of modern horizontal axis wind turbines. To ensure the wind turbine is producing the maximum amount of electric energy at all times, the yaw drive is actively controlled to keep the rotor facing into the wind as the

wind direction changes. This is accomplished by measuring the wind direction by a wind vane situated on the back of the nacelle.

## 3.2 System Setup

The Wind Energy Conversion System consists of a variable speed wind turbine, Permanent Magnet Synchronous Generator (PMSG), three phase diode bridge rectifier and a boost converter. The wind turbine converts the kinetic energy into mechanical energy. The wind turbine system can be fixed speed wind turbine (FSWT) or variable speed wind turbine (VSWT). The main advantage of FSWT is the reduction in the power electronic converters that is expensive. But since the rotor speed is constant, the turbines cannot operate at peak efficiency. In VSWT, the turbine speed varies with wind speed so that maximum power can be extracted. The kinetic energy of the wind is converted to electrical energy through an electric generator connected to the wind turbine. The generators used can be PMSG or induction generators. Three types of induction generators are often used namely cage rotor, wound rotor with slip control and doubly fed induction generator. Compared with induction generator, PMSG has the advantage, it does not require external excitation system, there is no copper loss in the rotor circuit, low maintenance cost, high air gap flux density, better reliability, high torque to inertia ratio and high performance. The output of direct driven PMSG is rectified and it is boosted by a DC DC converter.

The output power from wind turbine can be controlled within a specific range of wind speeds bounded by cut-in ( $v_{cutin}$ ) and cut out ( $v_{cutout}$ ) speeds. At very low wind speeds, there is insufficient torque exerted by the wind on the turbine blades to make them rotate. However, as the speed increases, the wind turbine will begin to rotate and generate electrical power. The speed at which the turbine first starts to rotate and generate power is called the cut-in speed. As the speed increases above the rated output wind speed, the forces on the turbine structure continue to rise and at some point, there is a risk of damage to the rotor. As a result, a braking system is employed to bring the rotor to a standstill. This is called the cut-out speed. The rated power  $P_{rat}$  is obtained from the wind turbine at rated wind speed. There are four main operating regions as shown in Fig. 3.2.

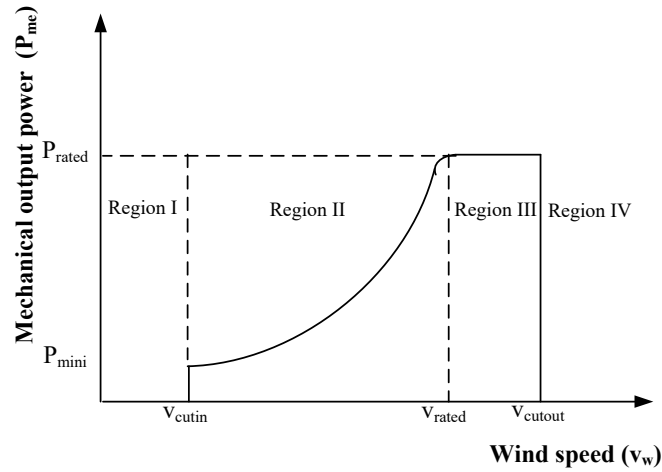


Figure 3.2: Typical power speed curve relationships in variable speed wind turbines

The first region is below  $v_{cutin}$  and the fourth region is above  $v_{cutout}$  where turbine is stopped and disconnected from grid. The second region is in between  $v_{cutin}$  and rated wind speed where the turbine can be operated to extract maximum energy. At higher wind speeds, i.e. in the third region, the turbine is designed to limit the power to this maximum level so that there is no further rise in the output power.

### 3.3 MPPT Algorithms

Maximum power point tracking algorithms are used to extract maximum power from the available wind energy and they can be categorised into tip speed ratio (TSR) control, power signal feedback (PSF) control and Hill Climb Search (HCS) control. In TSR control method, the rotational speed of generator is adjusted to maintain the optimum TSR. Optimum speed of generator is calculated by using wind velocity, turbine rotating speed and optimal TSR. The algorithm requires the knowledge of TSR optimum, the measurement of wind speed and turbine speed and is system dependent. Anemometers are mounted at different heights to register the wind speeds and the wind direction is indicated by wind vanes. In PSF control method, wind turbine operates at optimal operating point by using the prior knowledge of turbine's maximum power curve. The drawback is that there is no accurate way to determine  $K_{opt}$  since blade aerodynamic can change significantly overtime. In HCS method, an arbitrary small perturbation is

given to the one of the independent variables of the system and the next perturbation is based on the changes in the output power due to preceding perturbation. The HCS method has the advantage of no need of the measurement of wind speed or generator speed and independent of system characteristics. The drawback of this is slow tracking response, especially for high inertia systems.

### 3.4 Wind Turbine Modeling

The power of the wind is calculated in the following way.

$$P_{ke} = \frac{1}{2}mv_w^2 \quad (3.1)$$

where,

$P_{ke}$  = power contained in wind (J/s or W)

$m = \rho Av_w$  is mass flow rate

$\rho$  = air density ( $kg/m^3$ )

$A$  = area swept by rotor blades ( $m^2$ )

$v_w$  = wind speed (m/s)

Air is not a solid mass but a fluid, so  $m$  can be substituted by  $\rho Av_w$  then (3.1) becomes

$$P_{ke} = \frac{1}{2}(\rho Av_w)v_w^2 = \frac{1}{2}\rho Av_w^3 \quad (3.2)$$

The density of air varies with the height above sea level and temperature. The standard value of density used is  $1.25 \text{ kg/m}^3$ .

Coefficient of power ( $C_p$ ) of a wind turbine is the measure of its efficiency in the conversion of wind energy into useful mechanical energy and is given by

$$C_p = \frac{\text{Mechanical output power of turbine}}{\text{Power contained in the wind}} \quad (3.3)$$

$C_p$  is a function of tip speed ratio ( $\lambda$ ) and pitch angle ( $\beta$ ). The maximum value of  $C_p$  is 0.59 which is known as Betz limit.

Tip speed ratio ( $\lambda$ ) is given by

$$\lambda = \frac{\text{Tangential speed at the tip of the blade}}{\text{Speed of the wind}} \quad (3.4)$$

$$\lambda = \frac{\omega_m R}{v_w} \quad (3.5)$$

where  $w_m$  is the speed of the turbine,  $R$  is the radius of the turbine.

$C_p$  is modeled by aerodynamic principles for turbine blade design [11].

$$C_p(\lambda, \beta) = C_1 \left[ \frac{C_2}{\lambda_i} - C_3\beta - C_4 \right] e^{\frac{-C_5}{\lambda_i}} + C_6\lambda \quad (3.6)$$

where

$$\frac{1}{\lambda_i} = \frac{1}{\lambda + 0.008\beta} - \frac{0.035}{\beta^2 + 1} \quad (3.7)$$

and the constants are  $C_1 = 0.5176$ ;  $C_2=116$ ;  $C_3 = 0.4$ ;  $C_4 = 5$ ;

$C_5 = 21$ ;  $C_6 = 0.0068$ ;

The turbine output power  $P_{me}$  is determined by

$$P_{me} = \frac{1}{2} \rho A C_p v_w^3 \quad (3.8)$$

$$T_{me} = \frac{P_{me}}{\omega_m} \quad (3.9)$$

$T_{me}$  is mechanical output torque.

The graph between  $C_p$  and tip speed ratio is plotted in Fig. 3.3. The value of  $C_{pmax}$

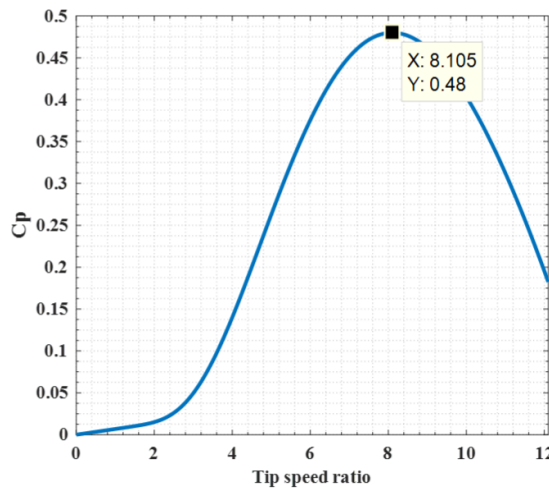


Figure 3.3:  $C_p$  versus tip speed ratio

is 0.48 and the tip speed ratio is 8.1. The graph between mechanical output power and turbine speed at various wind speeds are plotted in Fig. 3.4. From Fig. 3.4, it can be

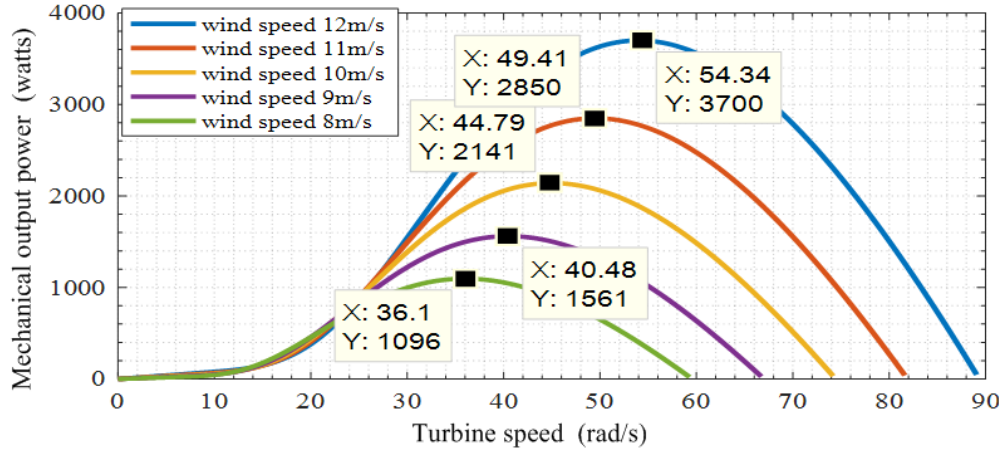


Figure 3.4: Mechanical output power versus turbine speed

found that the turbine speed and the power captured by the turbine changes with the wind velocity. For a particular wind speed, there is a certain turbine speed at which power is maximum. For achieving maximum power, the rotor speed should be at that optimum speed using MPPT technique. To extract maximum power from the wind, optimum torque control strategy is employed. The control strategy is illustrated in 3.5.

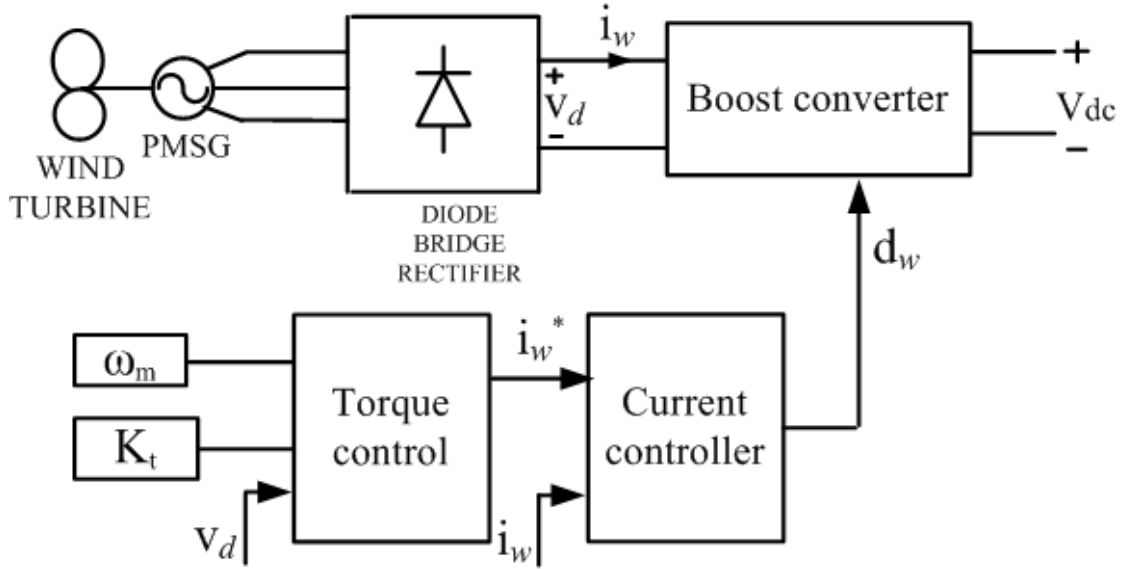


Figure 3.5: Optimum torque control of wind turbine system



### 3.5 Optimum Torque Control Strategy

The optimum torque control strategy is based on

$$\lambda_{opt} = \frac{\omega_{mopt} R}{v_w} \quad (3.10)$$

where  $\omega_{mopt}$  is the optimal speed of turbine under MPPT condition,  $\lambda_{opt}$  is the optimum tip speed ratio,  $R$  is the radius of rotor and  $v_w$  is the wind speed.

From (3.8), (3.9) and (3.10)

$$T_{opt} = \frac{\rho \pi R^5 C_{pmax} \omega_{opt}^2}{2 \lambda_{opt}^3} \quad (3.11)$$

$$T_{opt} = K_{opt} \omega_{opt}^2 \quad (3.12)$$

$$P_{opt} = T_{opt} \omega_{opt} \quad (3.13)$$

$$i_w^* = P_{opt} / v_d \quad (3.14)$$

The current corresponding to optimum torque,  $i_w^*$  is compared with the output current of rectifier  $i_w$  through a hysteresis current controller. The duty to the boost converter  $d_w$  is varied to get the maximum power. The torque developed by PMSG and the rotor speed is proportional to the output voltage and current. Thus perturbing or varying the output voltage will cause change in rotor speed. The variation of rotor speed at different wind speeds during MPPT operation are plotted in Fig. 3.6. From the Fig. 3.6 the rotor speed for wind speeds (8, 9, 10, 11, 12) m/s obtained are (36, 40, 44, 49, 54) rad/s respectively. The  $C_p$  is maximum and its value is 0.48 at various wind speeds indicating maximum power extraction.

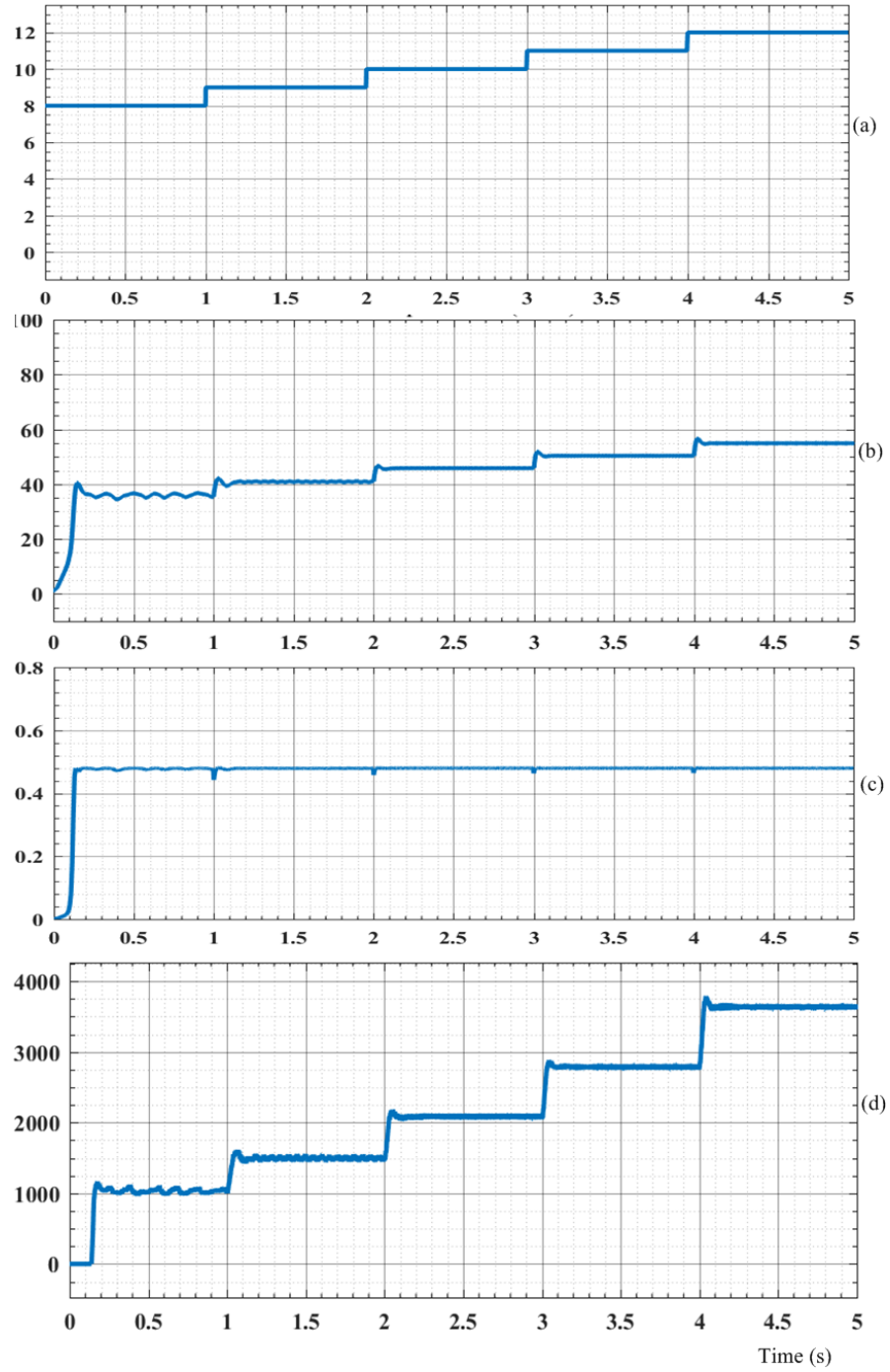


Figure 3.6: (a) Wind speed (m/s) (b) rotor speed (rad/s) (c)  $C_p$  coefficient (d) wind output power (watts)

### 3.6 Permanent Magnet Synchronous Generator Modeling

In the PMSG, the rotor magnetic flux is generated by permanent magnets, and therefore these generators are brush less type. Because of the absence of the rotor windings, a high power density can be achieved, reducing the size and weight of the generator. In addition, there are no rotor winding losses, reducing the thermal stress on the rotor. The drawbacks of these generators are that permanent magnets are more expensive and prone to demagnetization. Depending on how the permanent magnets are mounted on the rotor, the PMSG can be classified into surface-mounted and inset PM generators. In surface-mounted PMSG, the permanent magnets are placed on the rotor surface. In the inset PMSG, the permanent magnets are inset into the rotor surface.

Consider the simplified equivalent circuit [12] of PMSG based on d-q synchronous reference frame as shown in Fig. 3.7. The voltage equations of PMSG are given by

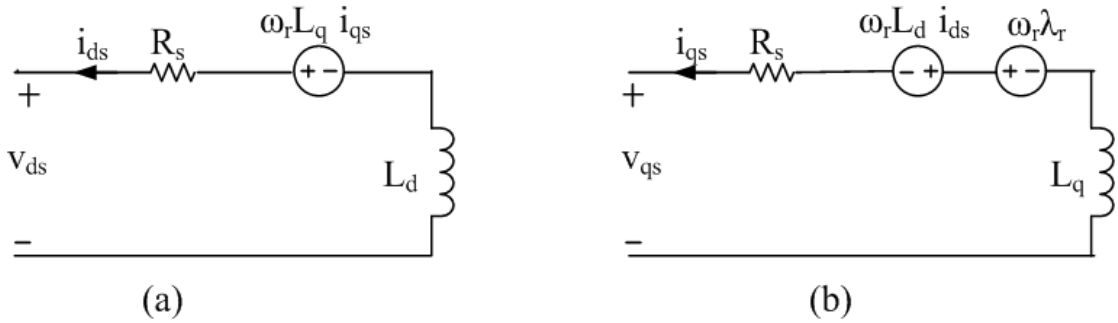


Figure 3.7: (a) d-axis circuit (b) q-axis circuit

$$v_{ds} = -R_s i_{ds} + \omega_r L_q i_{qs} - L_d p i_{ds} \quad (3.15)$$

$$v_{qs} = -R_s i_{qs} - \omega_r L_d i_{ds} + \omega_r \lambda_r - L_q p i_{qs} \quad (3.16)$$

The electromagnetic torque equation is given by

$$T_e = 1.5p[\lambda_r i_{qs} - (L_d - L_q) i_{ds} i_{qs}] \quad (3.17)$$

where  $L_q$  is q-axis inductance,  $L_d$  is d-axis inductance,  $R_s$  is the resistance of stator windings,  $i_{qs}$  is q-axis stator current,  $i_{ds}$  is d-axis stator current,  $v_{ds}$  is d-axis stator

voltage,  $v_q$  is q-axis stator voltage,  $\omega_r$  is angular velocity of the rotor,  $\lambda_r$  is the amplitude of flux induced,  $p$  is the number of pole pairs.

Assuming d-axis and q-axis inductances are equal  $L_d = L_q = L$  as in the case of non-salient synchronous generator, the electromagnetic torque is given by

$$T_e = 1.5p\lambda_r i_{qs} \quad (3.18)$$

The drive train for turbine-generator is considered as one lump mass model and is given as

$$J \frac{d\omega_r}{dt} = T_m - T_e - F\omega_r \quad (3.19)$$

$$\frac{d\theta_r}{dt} = \omega_r \quad (3.20)$$

where  $J$  is inertia of rotor,  $F$  = frictional coefficient of rotor,  $\theta_r$  = rotor angle.

### 3.7 Summary

This chapter deals with the structure of wind turbine, modeling of wind turbine and optimum torque based mppt strategy. The variation of rotor speed and wind power with wind speed is analysed using optimum torque control based mppt technique. The coefficient of power  $C_p$  is  $C_{pmax}$  for various wind speeds during mppt operation.

## CHAPTER 4

### HYBRID ENERGY STORAGE CONTROL AND POWER MANAGEMENT STRATEGY

In hybrid microgrid systems, the RES power is highly fluctuating as well as the common domestic load also varies severely. Therefore the microgrid load demand has to be supplied by both steady average component of power as well as peak power surges over a period of time. Hence microgrid requires energy storage devices with high energy density to supply average demand for a longer time and high power density devices to supply power spikes. Certain loads like motor loads, air conditioner need high starting current for few seconds only. Sizing a battery for this high current demand proves costly. The Ragone plot as shown in Fig. 4.1. is a chart used for performance comparison

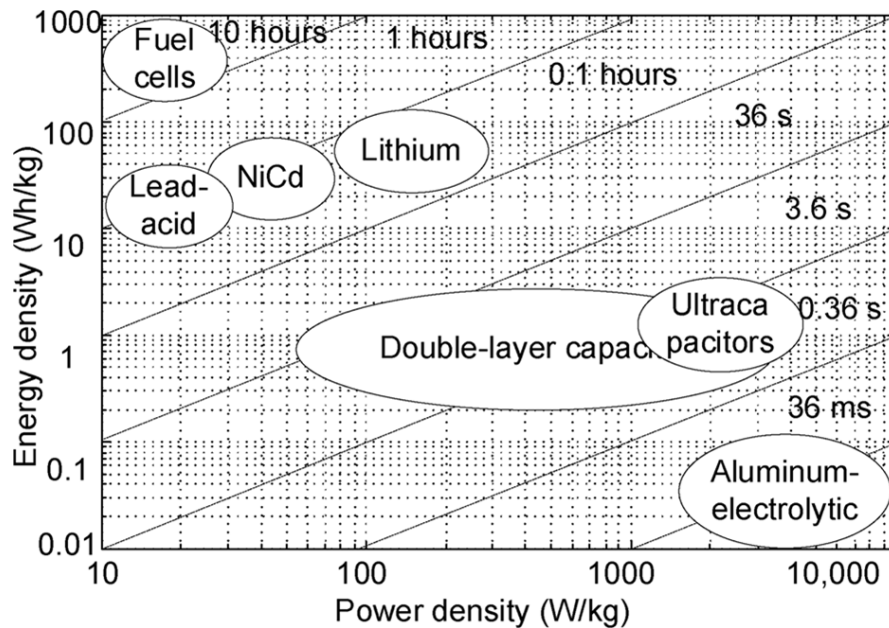


Figure 4.1: The Ragone plot [13]

of various energy storing devices where the values of energy density (in Wh/kg) are plotted versus power density (in W/kg). The BES systems have high energy density, low power density, low self discharge, low cycle life, long charge times, relatively lower cost per kWh. The supercapacitor systems have low energy density, high power density, high cycle life, very high self discharge, short charge times, high cost per Wh. So a

combination of battery with high energy density and a supercapacitor with high power density can be used to meet the load demand.

## 4.1 Hybrid Energy Storage and Control

The control scheme for hybrid energy storage system for effective dc link voltage stabilisation is shown in Fig. 4.2. The DC link voltage is maintained with respect to its

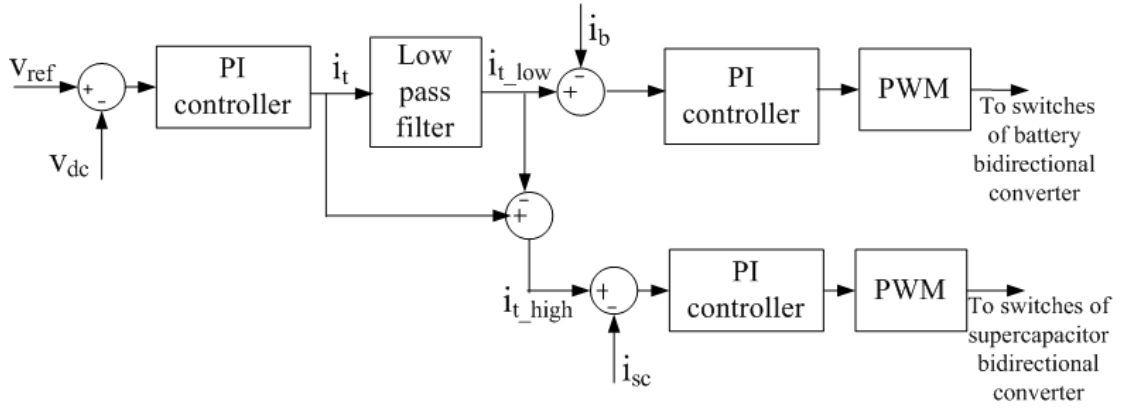


Figure 4.2: Control system for hybrid energy storage

reference value by means of a closed loop controller. The difference between reference voltage and DC bus voltage is given to the proportional integral (PI) controller. The  $i_T$  obtained is the total current required to stabilise the DC link voltage. The  $i_T$  is filtered into low frequency component with a low pass filter of cut-off frequency 5 Hz ( $\frac{1}{T_c}$ ).

$$\Delta v_{dc} = v_{ref} - v_{dc} \quad (4.1)$$

$$i_T = K_p \Delta v_{dc} + K_i \int \Delta v_{dc} dt \quad (4.2)$$

$$i_{elow} = f_{LPF}(i_T) = \frac{1}{1 + sT_c} i_T \quad (4.3)$$

$$i_{ehigh} = i_T - i_{elow} \quad (4.4)$$

where  $\Delta v_{dc}$ ,  $v_{ref}$ ,  $v_{dc}$ ,  $i_{elow}$ ,  $i_{ehigh}$ ,  $K_p$ ,  $K_i$  are the instantaneous variables representing the transient change, reference and actual values of dc link voltage, low frequency and high frequency components of error current, dc link PI controller gains respectively.

The low frequency component is given as reference to the battery current loop and the high frequency component is the reference to the supercapacitor current loop. In this a bidirectional buck-boost converter is used. The controller is designed by considering the boost mode of operation [14]. The gating pulses to the switches of converter is the pulse width modulated output from PI controller of inner current loop. The battery current controller is designed for 1/10th of switching frequency (1.5 kHz). The voltage controller bandwidth (50 Hz) is taken lesser than the right half plane zero frequency of supercapacitor converter. The system is designed with sufficient phase margin to reduce the amount of overshoot and ringing and also considering stability requirements [15]. The transient response time of the system can be shortened by increasing the feedback loop cross over frequency. The amount of overshoot and ringing allowed in the transient response can be limited by having a large phase margin.

## 4.2 Bidirectional DC DC Converters

The bidirectional DC-DC converter allows current to flow in both directions. Fig 4.3.

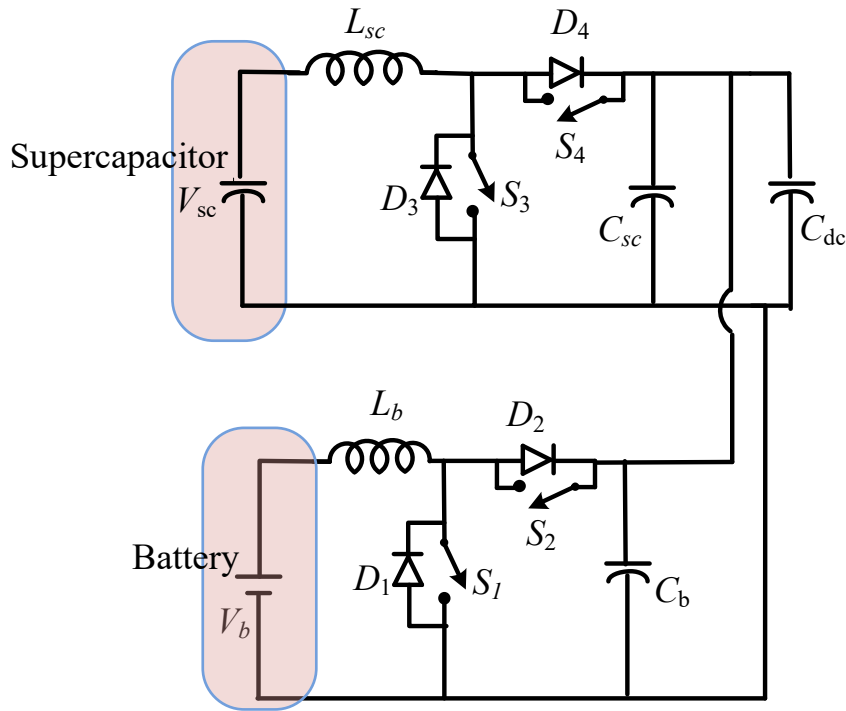


Figure 4.3: Bidirectional converter with battery and supercapacitor

shows the circuit diagram of DC-DC bidirectional converter connected to battery and

supercapacitor. It is a combination of boost stage together with a buck stage connected antiparallel to each other. When switch S1/S3 and diode D2/D4 are operated, the bidirectional converter operates in boost mode and power flows from storage unit to DC bus (discharging). When S2/S4 and diode D1/D3 are operated, the bidirectional converter needs to be operated in buck mode and power flows from DC bus to storage unit (charging). In boost mode battery/supercapacitor voltage is stepped up and the DC bus voltage is controlled at required level of 400 V. The buck stage allows charging of battery/supercapacitor with required current and voltage level from DC bus.

### 4.3 Design of PI Controller for HESS

According to [16], the discharging and charging of bidirectional converter share the same converter transfer function, therefore a unified controller can be used. A unified controller means both the switches are controlled in a complementary fashion using a single controller. Here boost mode of operation is used for designing the controller. The voltage control loop is made slower than the current control loop. The design of current controller for supercapacitor and battery converter and voltage controller are explained in subsequent subsections.

#### 4.3.1 Supercapacitor Current Controller

The block diagram representation of supercapacitor controller is shown in Fig. 4.4.

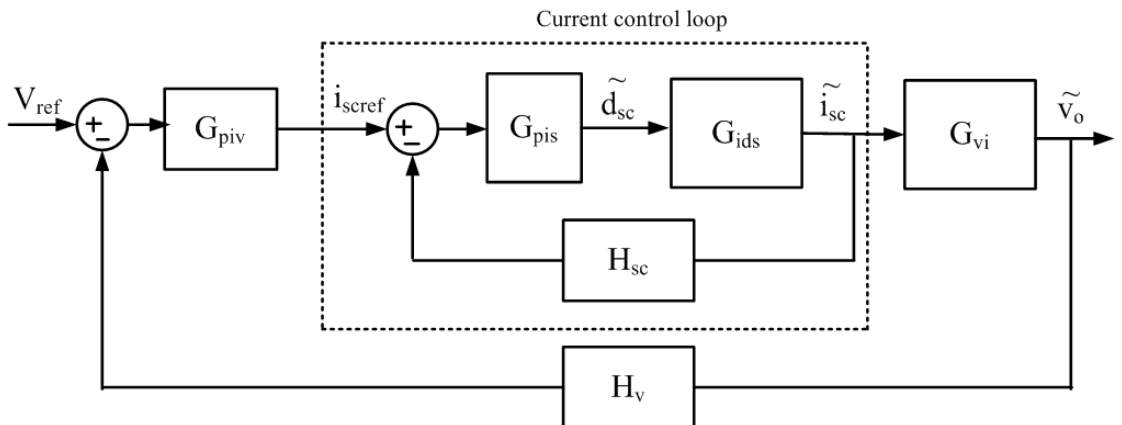


Figure 4.4: Block diagram of supercapacitor controller

$$V_g = V_{sc} = 64 \text{ V};$$



$$V_o = 400 \text{ V};$$

$$\frac{V_o}{V_g} = \frac{1}{1 - D_{sc}} \quad (4.5)$$

$$D_{sc} = 0.84;$$

From (2.14) and assuming 1 % ripple in the output voltage

$$0.01 = \frac{0.84}{15 * 10^3 * 20 * C_{sc}}; \quad (4.6)$$

$$C_{sc} = 280 \mu\text{F}$$

From (2.12) and assuming 10 % ripple in the inductor current

$$0.1 = \frac{(1 - 0.84)^2 * 0.84 * 20}{L_{sc} * 15 * 10^3} \quad (4.7)$$

$$L_{sc} = 0.286 \text{ mH};$$

The transfer function for current controller is given as

$$G_{ids} = \frac{\tilde{i}_{sc}}{\tilde{d}_{sc}} = \frac{V_o C_{sc} s + 2 \frac{V_o}{R}}{L_{sc} C_{sc} s^2 + \frac{L_{sc}}{R} s + (1 - D_{sc})^2} \quad (4.8)$$

where  $\tilde{i}_{sc}$  and  $\tilde{d}_{sc}$  are small perturbations in the inductor current and duty ratio of supercapacitor converter.

$$G_{ids} = \frac{0.112s + 40}{8.008 * 10^{-8} s^2 + 1.43 * 10^{-5} s + 0.0256} \quad (4.9)$$

The current controller bandwidth of supercapacitor is taken as 1/6th of switching frequency,

$$f_c = \frac{f_{sw}}{6} = \frac{15 * 10^3}{6} = 2.5 \text{ kHz} = 15707.96 \text{ rad/s} \quad (4.10)$$

At 15.7 krad/s the uncompensated loop gain has a magnitude of 39 dB and phase is  $-90.7^\circ$

To obtain a phase margin of  $77^\circ$ ;  $\angle \phi_{req} = -103^\circ$

$$\angle \phi_{req} = \angle G_{ids} + \angle \phi_{pi} \quad (4.11)$$

$$-103 = -90.7 + \angle \phi_{pi} \quad (4.12)$$

$$\angle \phi_{pi} = -12.3;$$

$$\angle \phi_{pi} = -90 + \tan^{-1} \frac{f_c}{f_L} \quad (4.13)$$

$$-12.3 = -90 + \tan^{-1} \frac{f_c}{f_L} \quad (4.14)$$

$$\omega_L = 3424.88 \text{ rad/s}$$

$$|G_{idsc}| = |G_{ids}| * |G_{pi}| \quad (4.15)$$

$$|G_{pi}| = K_{pis} \frac{\sqrt{f_L^2 + f_c^2}}{f_c} \quad (4.16)$$

$$|G_{idsc}| = 1$$

$$20 \log |G_{ids}| = 39 \text{ dB}$$

$$|G_{ids}| = 89.125$$

$$k_{pis} = 0.01096$$

The compensator for supercapacitor converter obtained is

$$G_{pis} = K_{pis} \left( \frac{s + \omega_L}{s} \right) \quad (4.17)$$

$$G_{pis} = K_{pis} + \frac{K_{ds}}{s} \quad (4.18)$$

$$K_{pis} = 0.01096 \text{ and } K_{ds} = 37.54$$

$$G_{pis} = 0.01096 + \frac{37.54}{s} \quad (4.19)$$

The open loop transfer function of the compensated current loop is given by

$$G_{idsc} = G_{pis} G_{ids} H_{sc} \quad (4.20)$$

where  $H_{sc}$  is the gain of current sensor and is taken as unity. The bode plot of current control loop of supercapacitor with and without compensator are shown in Fig. 4.5.

The phase margin obtained is  $77.1^\circ$  for a bandwidth of 2.5 kHz.

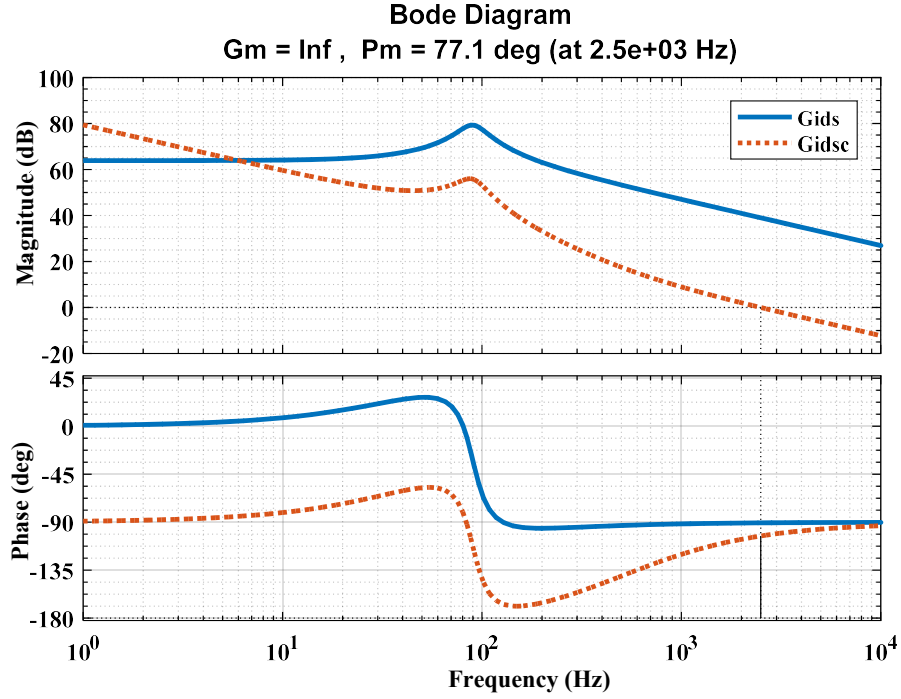


Figure 4.5: Bode plot of compensated (Gidsc) and uncompensated (Gids) supercapacitor current control loop.

### 4.3.2 Battery Current Controller

The block diagram for current controller of battery is shown in Fig. 4.7.

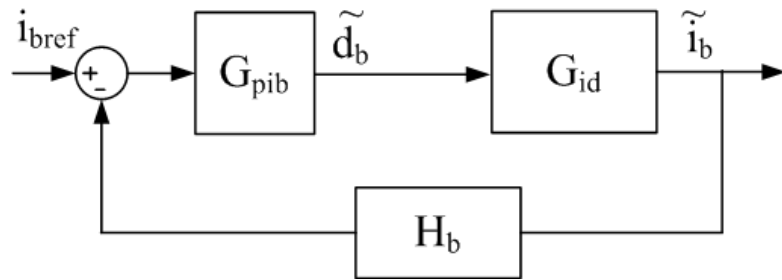


Figure 4.6: Block diagram of battery current controller

$$V_g = V_b = 192 \text{ V};$$

$$V_o = 400 \text{ V};$$

$$\frac{V_o}{V_g} = \frac{1}{1 - D_b} \quad (4.21)$$

$$D_b = 0.52;$$

From (2.14) assuming 1 % ripple in output voltage

$$0.01 = \frac{0.52}{15 * 10^3 * 20 * C_b}; \quad (4.22)$$

$$C_b = 173 \mu F$$

From (2.12) assuming 10% ripple in the inductor current

$$0.1 = \frac{(1 - 0.52)^2 * 0.52 * 20}{L_b * 15 * 10^3} \quad (4.23)$$

$$L_b = 1.59 \text{ mH};$$

The transfer function of inductor current to duty control for current controller is shown as

$$G_{id} = \frac{\tilde{i}_b}{\tilde{d}_b} = \frac{V_o C_b s + 2 \frac{V_o}{R}}{L_b C_b s^2 + \frac{L_b}{R} s + (1 - D_b)^2} \quad (4.24)$$

where  $\tilde{i}_b$  and  $\tilde{d}_b$  are small perturbations in the inductor current and duty ratio of battery converter respectively.

$$G_{id} = \frac{0.0692s + 40}{2.751 * 10^{-7} s^2 + 7.95 * 10^{-5} s + 0.2304} \quad (4.25)$$

The current controller bandwidth of battery is taken as 1/10th of switching frequency .

$$f_{c2} = \frac{f_{sw}}{6} = \frac{15 * 10^3}{10} = 1.5 \text{ kHz} = 9420 \text{ rad/s} \quad (4.26)$$

At 9420 rad/s the gain is 28.6 dB and phase is  $-91.7^\circ$

To get a phase margin of  $77^\circ$  ;

$$\angle \phi_{req} = -103^\circ$$

$$-103 = -91.7 + \angle \phi_{pi}$$

$$\angle \phi_{pi} = -11.3;$$

$$\angle \phi_{pi} = -90 + \tan^{-1} \frac{f_{c2}}{f_{L2}} \quad (4.27)$$

$$-11.3 = -90 + \tan^{-1} \frac{f_{c2}}{f_{L2}} \quad (4.28)$$

$$f_{L2} = 299 \text{ Hz}$$

$$\omega_{L2} = 1882.30 \text{ rad/s}$$

$$|G_{idc}| = |G_{id}| * |G_{pib}| \quad (4.29)$$

$$|G_{idc}| = 1$$

$$20 \log |G_{id}| = 28.6 \text{ dB}$$

$$|G_{id}| = 26.91$$

$$|G_{pib}| = K_{pib} \frac{\sqrt{f_{L2}^2 + f_{c2}^2}}{f_{c2}} \quad (4.30)$$

$$K_{pib} = 0.03644$$

The transfer function of the PI compensator is given by

$$G_{pib} = K_{pib} \left( \frac{s + \omega_{L2}}{s} \right) \quad (4.31)$$

$$G_{pib} = K_{pib} + \frac{K_{ib}}{s} \quad (4.32)$$

where  $K_{pib}$  and  $K_{ib}$  are the gains of the PI controller.

$$K_{pib} = 0.03644 \text{ and } K_{ib} = 68.59$$

$$G_{pib} = 0.03644 + \frac{68.59}{s} \quad (4.33)$$

The open loop transfer function of the compensated current loop is given by

$$G_{idc} = G_{pib} G_{id} H_b \quad (4.34)$$

where  $H_b$  is the gain of current sensor and its value is taken as unity.

The frequency response analysis of compensated and uncompensated battery current control loop is plotted in Fig. 4.7. The phase margin obtained is  $77^\circ$  for a bandwidth of 1.5 kHz.

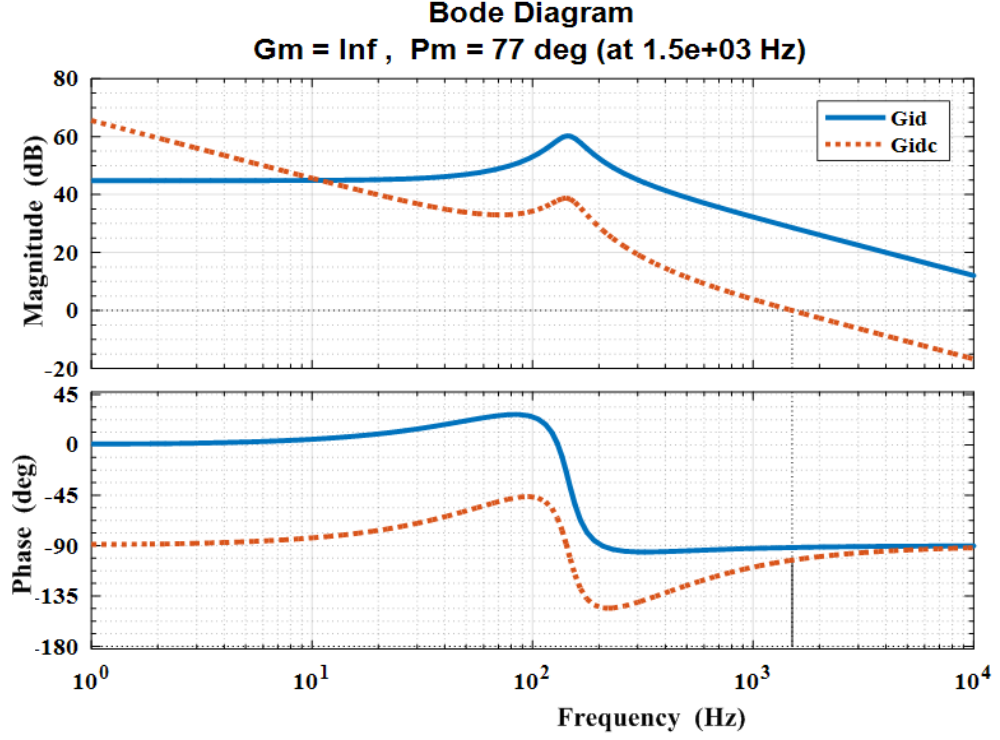


Figure 4.7: Bode plot of compensated (Gidc) and uncompensated (Gid) battery current control loop.

### 4.3.3 Voltage Controller

The transfer function of output voltage to inductor current for voltage control loop is given as

$$G_{vi} = \frac{\hat{v}_o}{\hat{i}_{sc}} = \frac{R(1 - D_{sc})(1 - \frac{L_{sc}}{R(1 - D_{sc})^2} s)}{2 + RC_{sc}s} \quad (4.35)$$

where  $\hat{v}_o$  and  $\hat{i}_{sc}$  are the small perturbations in the output voltage and input current of supercapacitor converter.

$$G_{vi} = \frac{-0.001787s + 3.2}{0.0056s + 2} \quad (4.36)$$

The transfer function of voltage control loop compensator is given by

$$G_{piv} = K_{pv} + \frac{K_{iv}}{s} \quad (4.37)$$

where  $K_{pv}$  and  $K_{iv}$  are gains of the PI controller.

$$G_{piv} = 0.505 + \frac{203.31}{s} \quad (4.38)$$

The open loop transfer function of the voltage control loop is given as

$$G_{vidc} = G_{piv}G_{clsc}G_{vi}H_v \quad (4.39)$$

where

$$G_{clsc} = \frac{G_{pis}G_{ids}}{1 + G_{pis}G_{ids}H_{sc}} \quad (4.40)$$

and  $H_v$  is the gain of the voltage sensor and its value is unity.

The open loop transfer function without compensator is given as

$$G_{vid} = G_{clsc}G_{vi}H_v \quad (4.41)$$

The right half plane zero frequency of supercapacitor converter is given by

$$f_{RHPZ} = \frac{(1 - D_{sc})^2 R}{2\pi L_{sc}} \quad (4.42)$$

$$f_{RHPZ} = \frac{(1 - 0.84)^2 * 20}{2\pi * 0.286 * 10^{-3}} = 285 \text{ Hz} \quad (4.43)$$

The voltage control loop is designed for  $\frac{f_{RHPZ}}{6}$  which is approximately 50 Hz.

The frequency response for compensated and uncompensated voltage control loop for a phase margin of  $76.5^\circ$  at a bandwidth of 50 Hz is shown in Fig. 4.8.

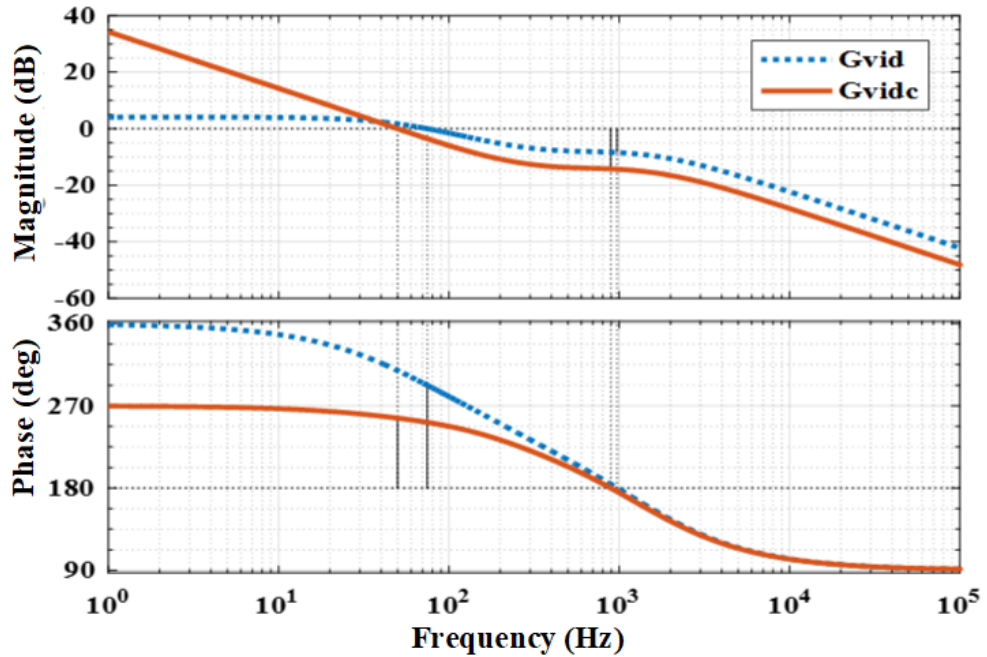


Figure 4.8: Bode plot for compensated ( $G_{vidc}$ ) and uncompensated ( $G_{vid}$ ) DC link voltage control loop.

## 4.4 State of Charge Estimation of Energy Storage System

The energy storage system undergoes frequent charging and discharging process during its usage. So the storage system has to be operated within their healthy state of charge limits. The SoC is estimated using coulomb's counting principle by considering initial SoC condition and current flowing through the storage device.

$$SoC_{ESS} = SoC_i - \frac{1}{3600C_{nom}} \int i_{ESS} dt \quad (4.44)$$

where  $SoC_{ESS}$ ,  $SoC_i$ ,  $C_{nom}$ ,  $i_{ESS}$  corresponds to SoC, initial value of SoC, nominal capacity, charging or discharging current of the energy storage units respectively.

## 4.5 Power Management Strategy

The power balancing between generation and load is achieved by a power management algorithm. This algorithm helps in preventing blackout, better supervision, effective utilization and better control between various microgrid elements. The overcharging/discharging of battery and supercapacitor is avoided by checking the SoC limits. The various inputs to the power management algorithm are  $P_{RES}$ ,  $P_L$ ,  $SoC_B$ ,  $SoC_{sc}$ ,  $i_{elow}$ ,  $i_{ehigh}$ ,  $I_{brat}$ ,  $I_{scrat}$  indicating the total photovoltaic and wind power, dc load power, state of charge of battery, state of charge of supercapacitor, low frequency (average) current component, high frequency current component, rated current of battery, rated current of supercapacitor. The charging, discharging and load shedding for power management is done by giving appropriate current references to battery and supercapacitor control loops. The power management algorithm assign  $i_{ehigh}$  to supercapacitor and  $i_{elow}$  to battery depending on the net power, SoC of battery and supercapacitor. The algorithm is based on the power balance equation

$$p_{pv(t)} + p_{w(t)} \pm p_{b(t)} \pm p_{sc(t)} - p_{loss(t)} = p_{L(t)} \quad (4.45)$$

where  $p_{pv(t)}$ ,  $p_{w(t)}$ ,  $p_{b(t)}$ ,  $p_{sc(t)}$ ,  $p_{L(t)}$ ,  $p_{loss(t)}$  are the instantaneous photovoltaic, wind, battery, supercapacitor, DC load power and total power loss in the microgrid respec-



tively. The  $\pm$  sign indicates bidirectional powerflow. The  $P_{net}$  is the difference between total renewable energy source power and load power. If the total renewable power is less than the load power, the mode of operation is deficit mode otherwise it is excess power mode. The supercapacitor is allowed to charge and discharge between a lower limit of 0.1 and a upper limit of 0.9 respectively. In deficit mode, the battery and supercapacitor bidirectional converter operates in discharging condition (buck) and will give necessary power to load. If battery state of charge is at lower limit (0.3), load shedding is required. In excess power mode, the bidirectional converter operates in charging (boost) mode and the ESS will get charged. If battery SoC has reached upper limit (0.9), the distributed source power is limited. The algorithm is implemented using MATLAB and the flowchart is shown in Fig. 4.9 .

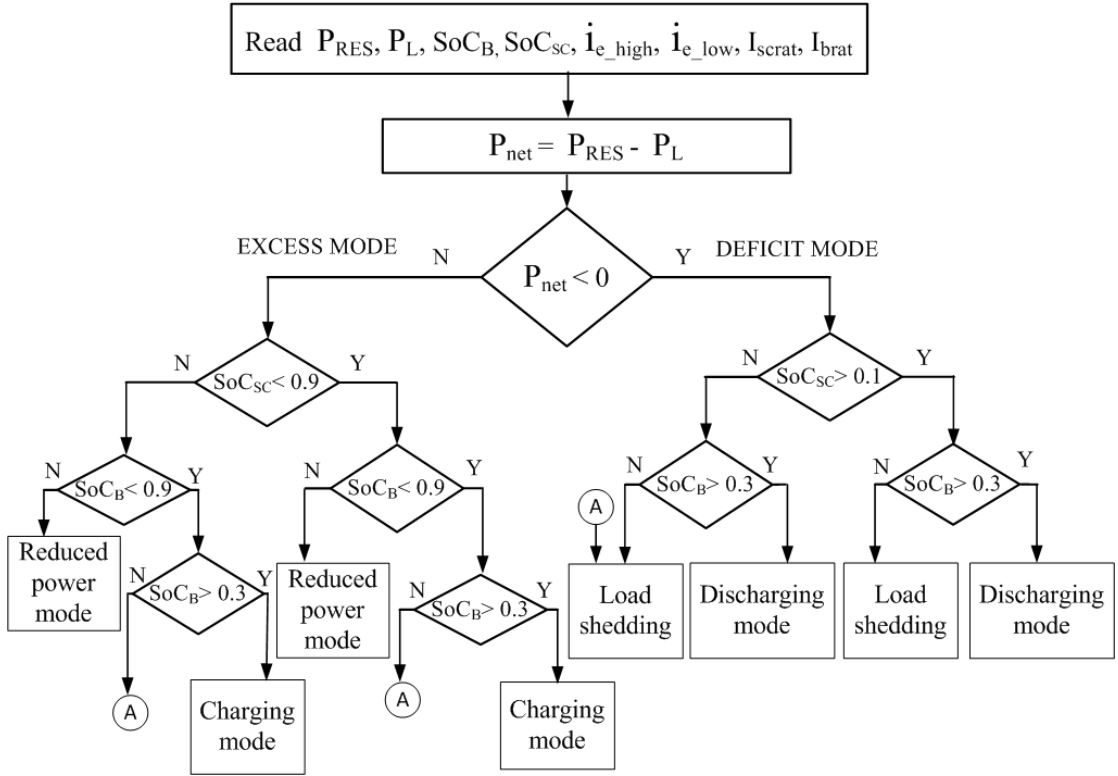


Figure 4.9: Flowchart for power management

## 4.6 Reduced Power Mode

The DC microgrid control can be centralised or decentralised. In centralised control the microgrid terminals are regulated by energy management using a centralised controller, which requires real time feedback and depends heavily on communication line. The

decentralised control approach, requires local measurements for power sharing with minimum communication requirements and is independent of a centralised controller. Droop control scheme is a classical decentralised control method which can be used on dc microgrids. The droop controller is a loop outside the current and voltage loop. The equation governing the conventional droop control is given by

$$V_{ref}^* = V_{ref} - i_o R_{dn} \quad (4.46)$$

where  $R_{dn}$  is the virtual droop resistance for  $n^{th}$  converter.  $V_{ref}$  is the output voltage reference at no load and  $i_o$  is the output current.

$$R_{dn} = \frac{\Delta V}{i_{maxn}} \quad (4.47)$$

$\Delta V$  is the maximum allowed voltage deviation,  $i_{maxn}$  is the maximum output current of  $n^{th}$  converter which depends on the maximum power of converter.

The droop control strategy is employed for load sharing among the renewable sources when the battery charges to its upperlimit (0.9). The distibuted sources are working in off-MPPT mode and voltage at the DC bus is constant. When the battery reaches the upper limit (0.9), the reduction of power is done by changing the control of duty reference from MPPT mode to droop controller mode. This is done by the power managment algorithm. The droop coefficients are designed [17] depending on the rating of PV and wind system. The droop coefficient for a voltage deviation of 1 V for PV of power rating 4.218 kW and for wind system of power rating 3.7 kW is obtained as follows.

$$i_{maxpv} = \frac{4218}{400} = 10.545 \text{ A} \quad (4.48)$$

$$R_{d1} = \frac{1}{10.545} = 0.0948 \text{ } \Omega \quad (4.49)$$

$$i_{maxwind} = \frac{3700}{400} = 9.25 \text{ A} \quad (4.50)$$

$$R_{d2} = \frac{1}{9.25} = 0.1081 \text{ } \Omega \quad (4.51)$$

The  $K_p$ ,  $K_i$  values for voltage controller obtained by trial and error method are 0.75, 6.44 and for current controller are 0.44, 2205 respectively. The control strategy is shown in Fig. 4.10.

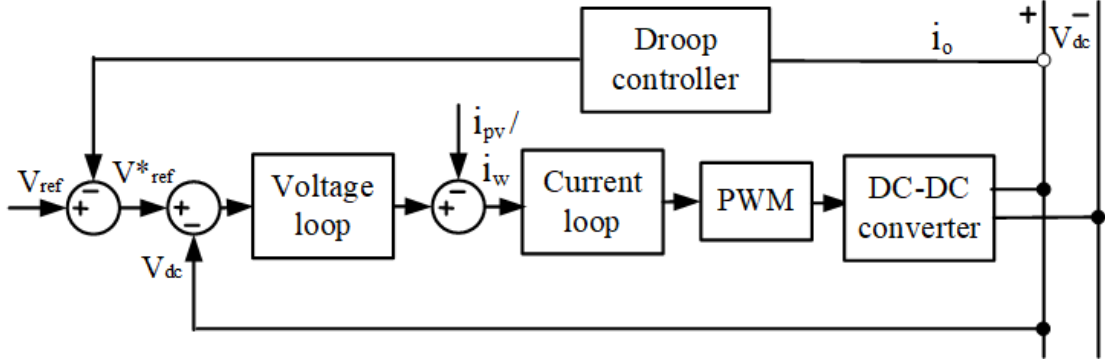


Figure 4.10: Droop control scheme in reduced power mode

## 4.7 Summary

The use of supercapacitor along with battery improves the performance and enhances the life of battery. The PI controller for hybrid energy storage systems are designed by frequency response analysis. The power between renewable generation and dc load is balanced by a power management algorithm by considering the SoC limits of battery and supercapacitor. During excess power condition and when battery reaches its upper SoC limit, the PV and wind power is reduced by droop control method.

# CHAPTER 5

## SIMULATION RESULTS

The proposed control strategy is tested for the microgrid system shown in Fig. 2.2 for four different cases in MATLAB-Simulink platform. In the results, the discharging and charging action of storage devices are indicated by positive and negative values respectively. The parameters used for simulation are shown in Table 5.1 .

### 5.1 Case (i): When both Solar Irradiation and Wind Speed Varies

The solar irradiance (1000, 850, 1000, 950, 1000, 0, 700, 900, 900)  $W/m^2$  and wind speed (12, 10, 11, 9, 12, 12, 10, 9, 0) m/s are changed at intervals of 1 s as shown in Fig. 5.1, Fig. 5.2 and Fig. 5.3. During time  $t = 0$  s to  $t = 4$  s, under excess power condition the battery is in charging state. From  $t = 0$  s to  $t = 1$  s the irradiation is 1000  $W/m^2$  and wind speed is 12 m/s, the corresponding solar power is 4218 W and wind power is 3700 W respectively. The load is 5000 W and the excess power is used to charge ESS. At  $t = 4$  s the load is suddenly changed from 5000 W to 10000 W. At this time, the solar power is 4218 W, wind power is 3700 W and the shortage of power to meet the load of 10000 W is supplied by ESS. From  $t = 4$  s to 9 s the system is operating in deficit mode. The DC bus voltage is within limit at  $t = 6$  s when irradiation increases from zero, with wind power already in the dc grid. The SoC of battery and supercapacitor increases during time  $t = 0$  s upto  $t = 4$  s and decreases from time  $t = 4$  s to 9 s. The tip speed ratio is 8.1 and  $C_p$  is  $C_{pmax}$  which is 0.48 for various wind speeds indicating MPPT operation. The PV and wind system is delivering maximum power corresponding to each solar irradiation and wind speed. The PV system uses perturb and observe algorithm and wind system uses optimum torque based control strategy for maximum power extraction. The DC bus voltage is maintained at 400 V for different solar irradiances and wind speeds.

Table 5.1: System Parameters

System	Parameter	Values
PV system	Maximum power point voltage and current	34.63 V, 4.35 A
	PV array maximum power	4.2 kW (7S, 4P)
	Short circuit current	4.85 A
	Open circuit voltage	43.6 V
	Reference solar irradiation	1000 W/m <sup>2</sup>
	Reference temperature	298 K
	Boost converter:	
	$L_p$	19.28 mH
	$C_p$	131 $\mu$ F
Wind system	Rated output power	3.7 kW
	Armature inductance	0.8 mH
	Stator phase resistance	12.25 m $\Omega$
	Number of pole pairs	4
	Rotor radius	1.8 m
	Optimum tip speed ratio	8.1
	$K_{opt}$	$32.82e^{-3}$ Nm/rad <sup>2</sup>
	Flux linkage	0.6
Energy storage system	<b>Lead Acid battery:</b>	
	Type	VRLA
	Voltage	192 V
	Capacity	200 Ah
	Bidirectional converter:	
	$L_b$	1.59 mH
	$C_b$	173 $\mu$ F
	<b>Supercapacitor:</b>	
	Rated capacitance	58 F
	Rated voltage	128 V
	Bidirectional converter:	
	$L_{sc}$	0.286 mH
	$C_{sc}$	280 $\mu$ F
	Switching frequency	15 kHz
DC bus	DC link voltage	400 V
	DC link capacitor	5000 $\mu$ F

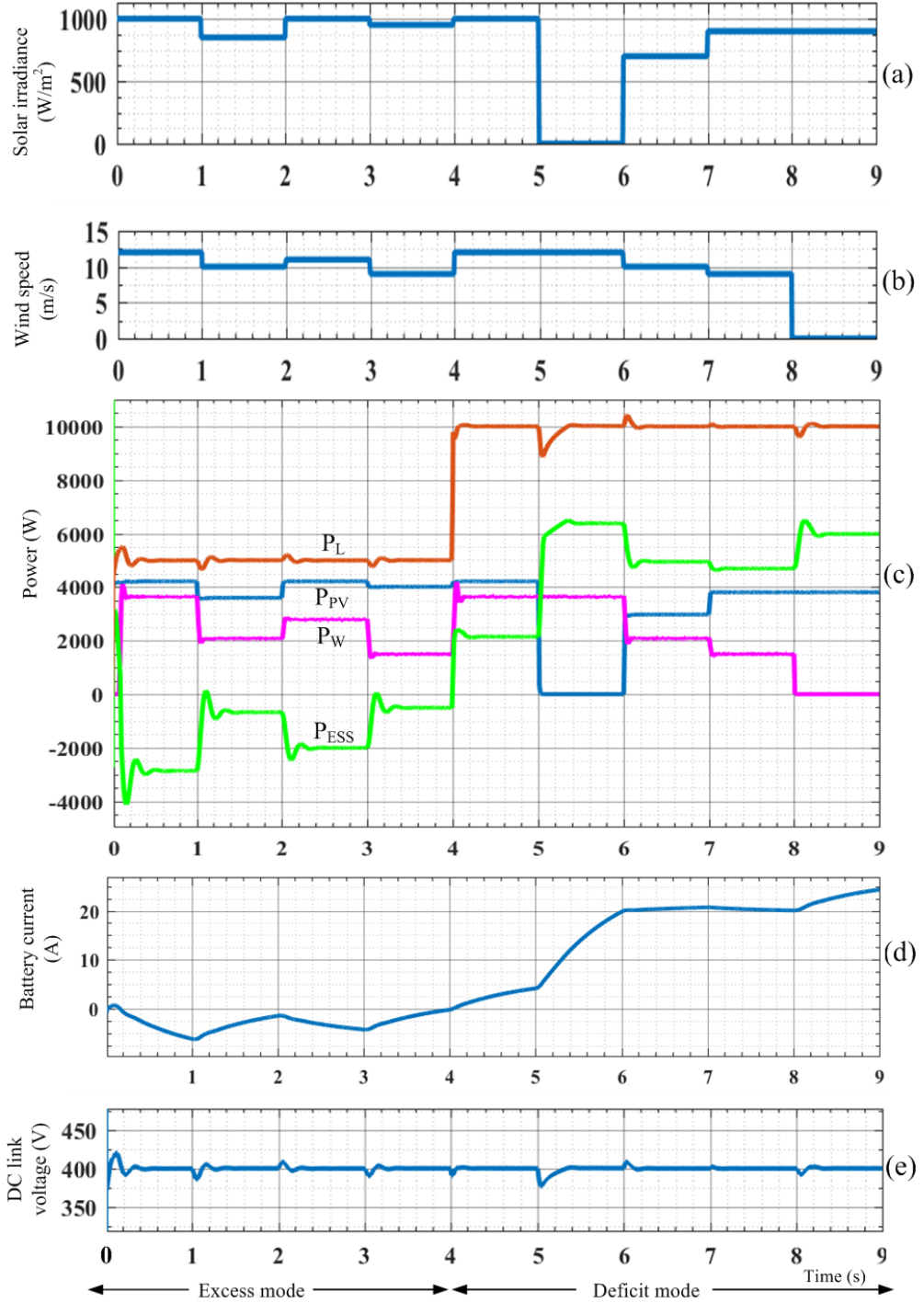


Figure 5.1: Performance under case (i): (a) Solar irradiance ( $\text{W/m}^2$ ) (b) wind speed (m/s) (c)  $P_L$ -load power,  $P_{pv}$ -PV power,  $P_w$ -wind power,  $P_{ESS}$ -energy storage system power (W) (d) battery current (A) (e) DC link voltage (V)

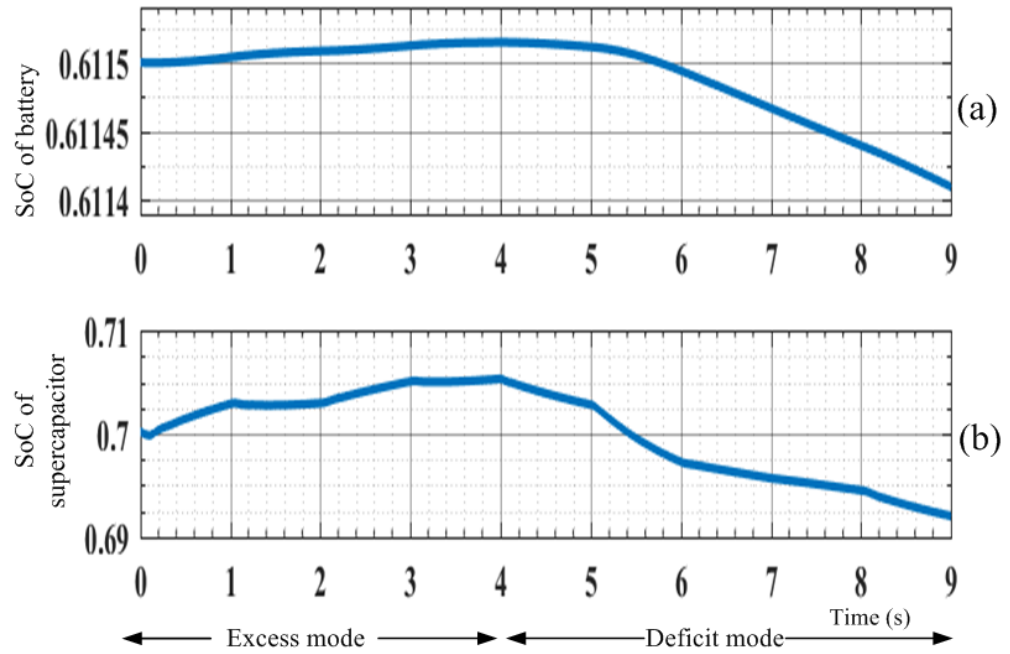


Figure 5.2: Performance under case (i): (a) SoC of battery (b) SoC of supercapacitor

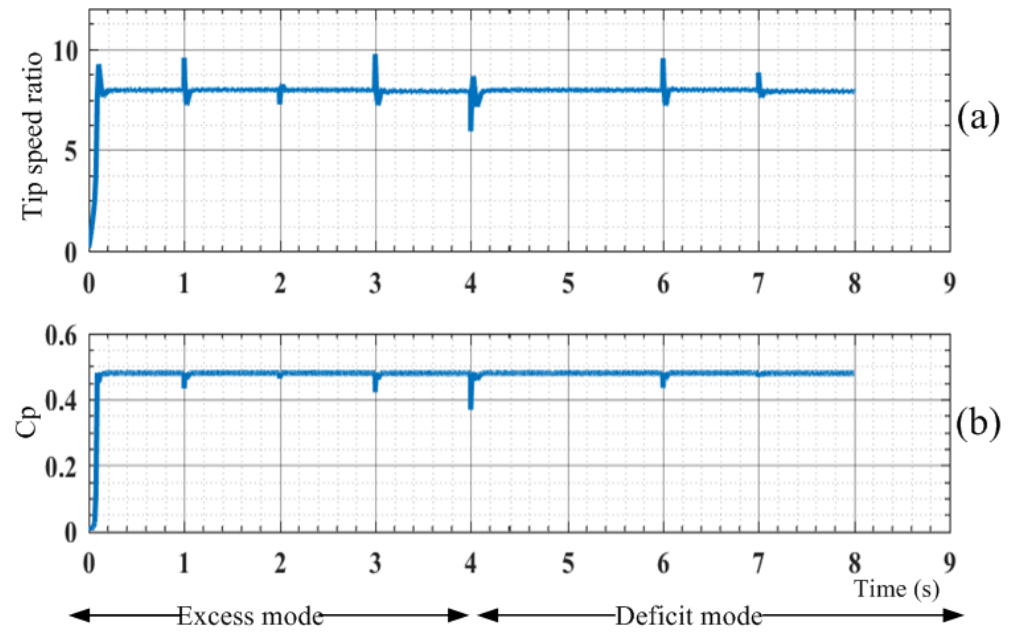


Figure 5.3: Performance under case (i): (a) Tip speed ratio (b) Cp coefficient

## 5.2 Case (ii): When SoC of Battery Varies

The SoC of battery is varied to test various cases in power management algorithm as shown in Fig. 5.4. and Fig. 5.5. The irradiance considered is  $1 \text{ kW/m}^2$  and wind speed

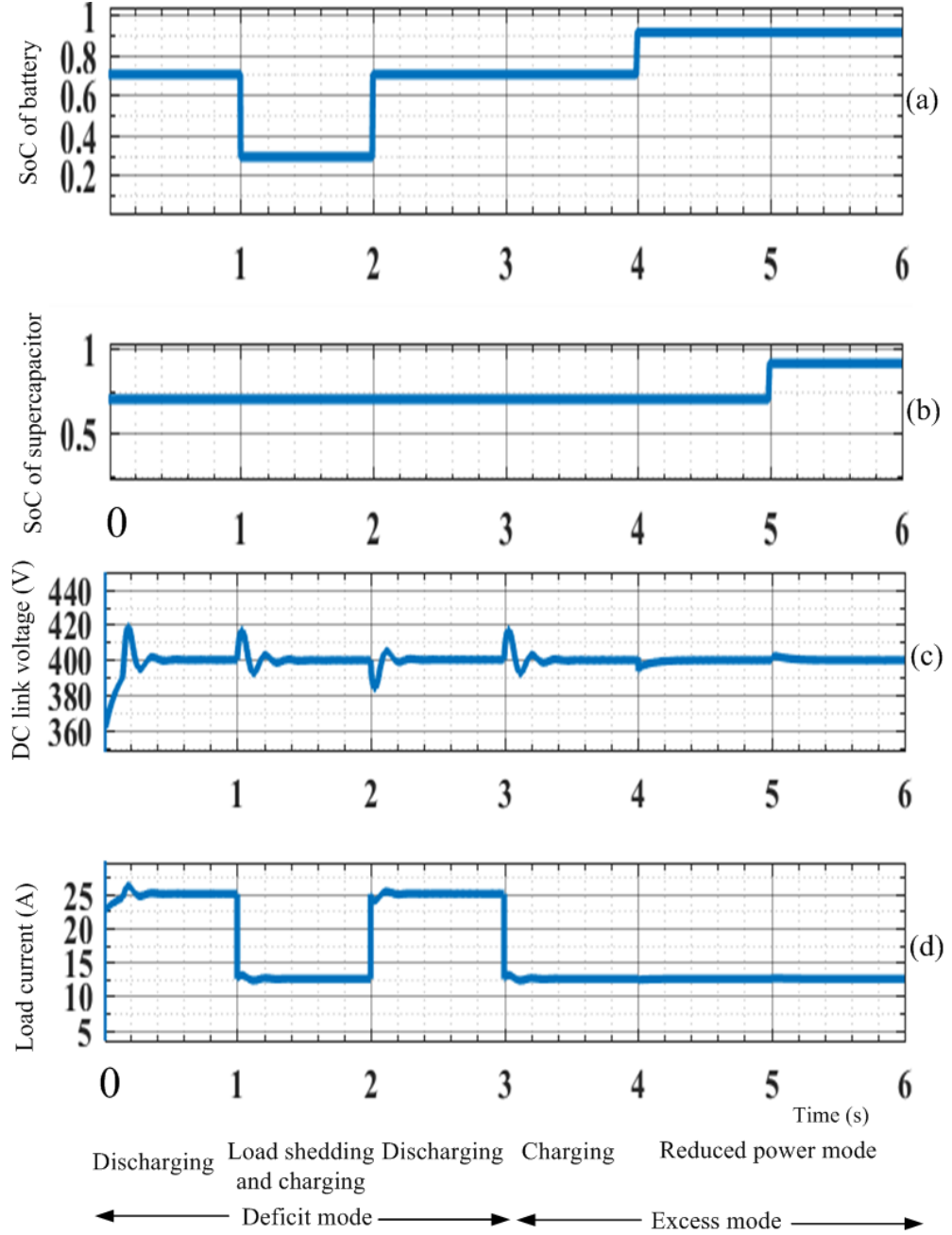


Figure 5.4: Performance under case (ii), variation of SoC of battery: (a) SoC of battery (b) SoC of supercapacitor (c) DC link voltage (V) (d) load current (A)

is  $12 \text{ m/s}$ . The system is operating in deficit mode from  $t = 1 \text{ s}$  to  $t = 3 \text{ s}$  and in excess power mode from  $t = 3 \text{ s}$  to  $t = 6 \text{ s}$ . The PV and wind system is operating in MPPT mode and is giving a power of  $4218 \text{ W}$  and  $3700 \text{ W}$  respectively. The battery and supercapacitor discharges to meet the load requirement ( $10000 \text{ W}$ ) upto  $1 \text{ s}$ . At  $t = 1 \text{ s}$  the



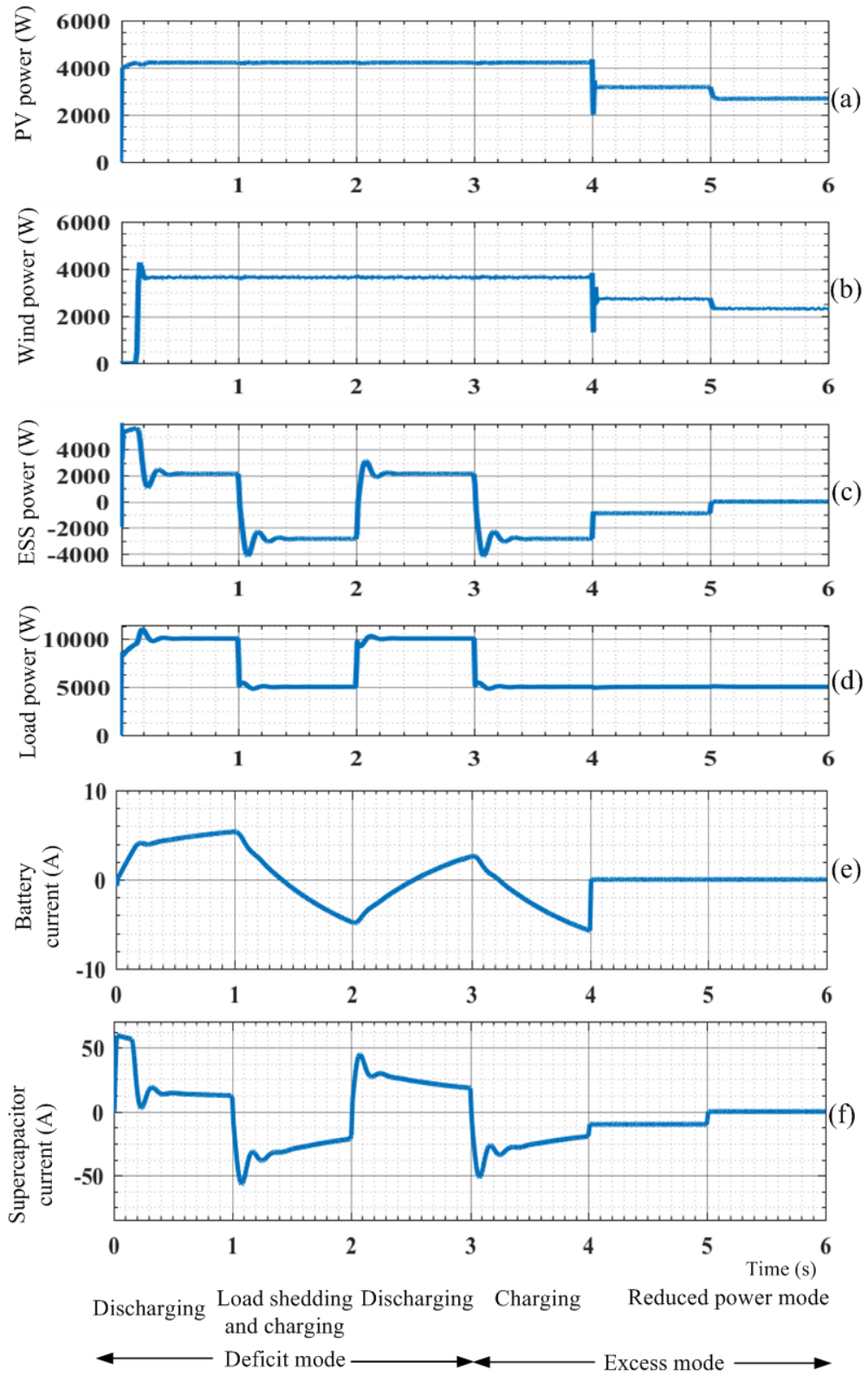


Figure 5.5: Performance under case (ii), variation of SoC of battery: (a) PV power (W) (b) wind power (W) (c) energy storage system power (W) (d) load power (W) (e) battery current (A) (f) supercapacitor current (A)

SoC of battery is at lower limit (0.3), further discharging of battery is not recommended and load shedding is implemented. The load current is reduced to 12.5 A and the load power is 5000 W. At  $t = 2$  s, SoC is changed to 0.7 and discharging of battery happens. The resistive load is changed to  $32 \Omega$  at  $t = 3$  s to enter into excess power condition. The PV power is 4218 W, wind power is 3700 W and load is 5000 W. The surplus power obtained is used to charge the battery and supercapacitor. At  $t = 4$  s the SoC of battery is changed to upper limit (0.9), so reduced power mode is enabled. In this mode, the system is operating in droop control mode and the DC bus voltage is within limits. The SoC of supercapacitor is at 0.7 and it is charged with rated current. The load power and the power required to charge supercapacitor is provided by PV and wind source. When the SoC of supercapacitor is changed to 0.9 at  $t = 5$  s, load of 5000 W and losses are shared by PV (2673 W) and wind (2337 W) respectively.

### 5.3 Case (iii): Pitch Angle Variation

In pitch controlled wind system, when the wind speed reaches very high (high  $P_w$ ), the power is reduced by controlling the pitch angle [18]. The purpose of pitch angle control is to prevent the mechanical input power to exceed the design limits and to minimize the fatigue loads of the turbine mechanical component. During normal operation the value of pitch angle is kept at  $0^\circ$  to extract maximum power from wind. From  $t = 0$  s to  $t = 1$  s the wind speed is 12 m/s, pitch angle  $\beta$  is  $0^\circ$  and wind power output is 3700 W. At  $t = 1$  s, the wind speed reaches 14.2 m/s, the pitch angle is varied from  $5^\circ$  to  $20^\circ$  at intervals of 1 s. The PV system is operating in mppt mode. The wind power got reduced by varying pitch angle. The load power is 5000 W. The dc link voltage is maintained at 400 V. The variation of pitch angle resulting in reduction of wind power is shown in Fig. 5.6.

### 5.4 Case (iv): Change in Load Resistance

The performance of the integrated system, when there is sudden change in load during excess power mode and deficit power mode is shown in Fig. 5.7. and Fig. 5.8. re-

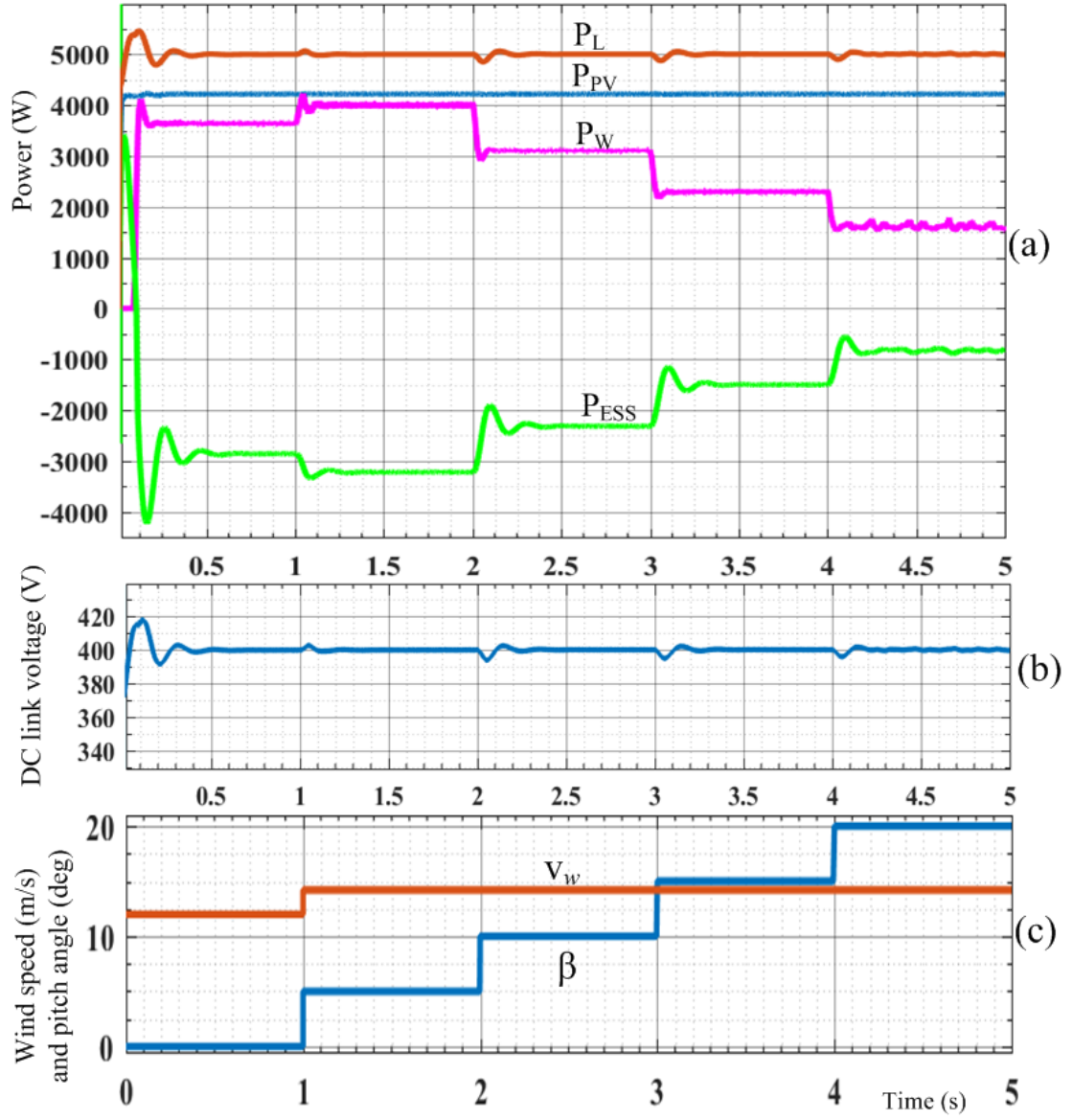


Figure 5.6: Case (iii): (a)  $P_L$ -load power,  $P_{PV}$ -PV power,  $P_W$ -wind power,  $P_{ESS}$ -energy storage system power (W) (b) DC link voltage (V) (c)  $v_w$  - wind speed (m/s),  $\beta$  - pitch angle (deg)

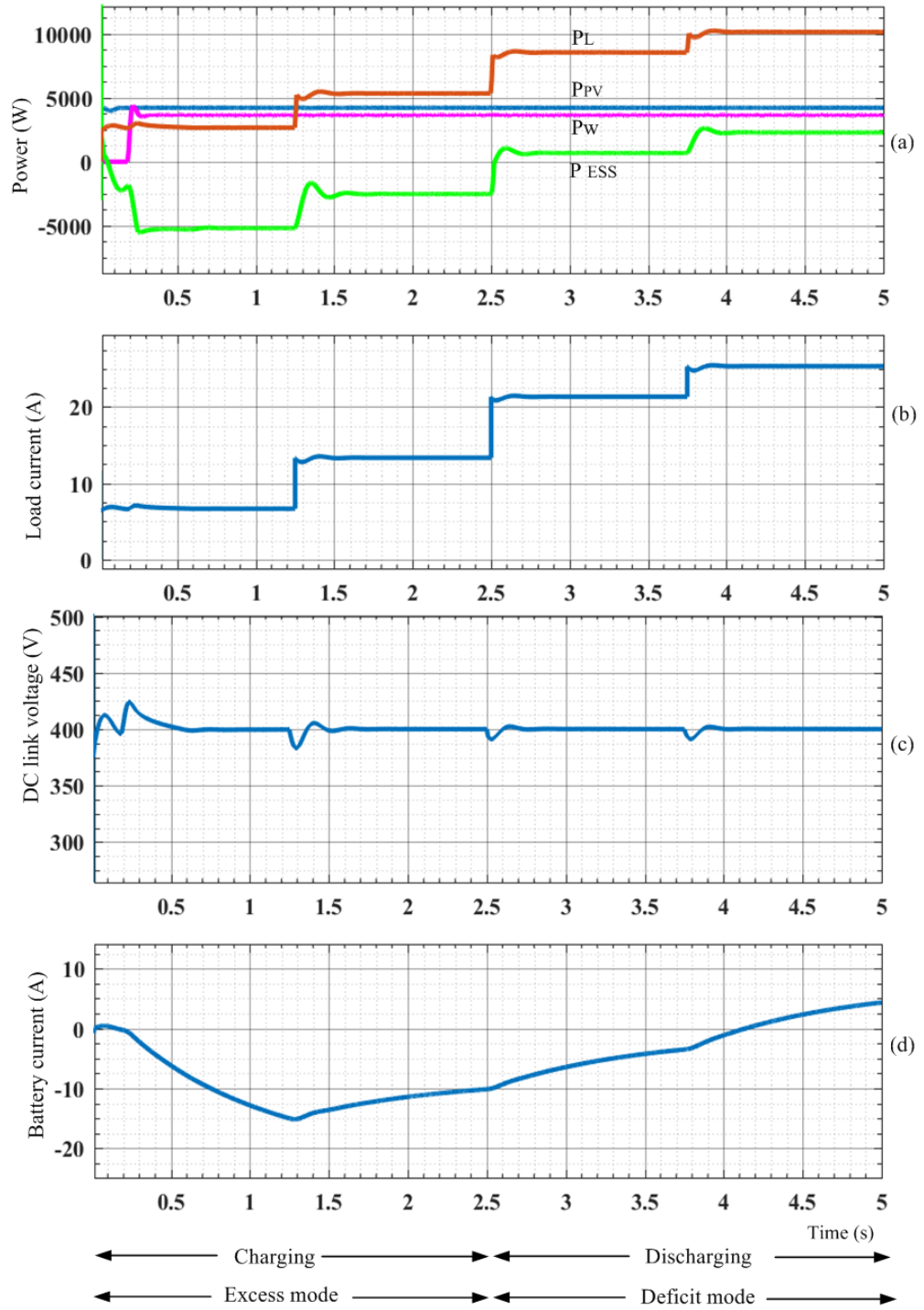


Figure 5.7: Case (iv): (a)  $P_L$ -load power,  $P_{PV}$ -PV power,  $P_W$ -wind power,  $P_{ESS}$ -energy storage system power (W) (b) load current (A) (c) DC link voltage (V) (d) battery current (A)

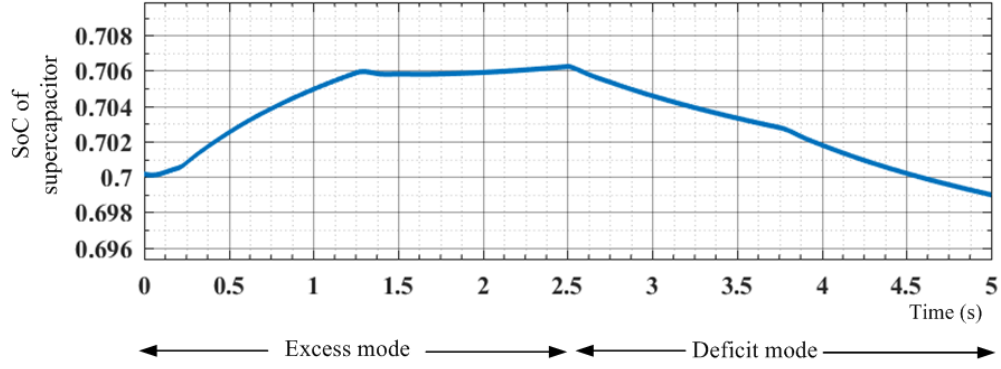


Figure 5.8: Case (iv): SoC of supercapacitor

spectively. The  $60 \Omega$  (2666 W) resistive load is changed to  $30 \Omega$  (5333 W) at  $t = 1.25$  s and to  $18.7 \Omega$  (8533 W) at  $t = 2.5$  s. At  $t = 3.75$  s the load is again changed to  $15.7 \Omega$  (10191 W). The dc grid voltage is maintained at 400 V for these sudden changes in load. The irradiance considered is  $1 \text{ kW/m}^2$  and wind speed is 12 m/s. The battery and supercapacitor charges during excess mode from  $t = 0$  s to  $t = 2.5$  s and discharges in deficit mode from 2.5 s to 5 s. The SoC of supercapacitor is increasing upto  $t = 2.5$  s indicating charging during excess power condition and SoC is decreasing from  $t = 2.5$  s indicates discharging action during deficit mode.

## 5.5 Summary

The solar and wind energy integrated with battery and supercapacitor is tested for various cases in MATLAB-Simulink platform. The integrated system is tested for sudden change in load, simultaneous variation in solar irradiance and wind speed, variation of SoC of battery and variation of pitch angle. The power management algorithm controls and regulates the flow of power and thereby keeps the DC grid voltage constant. The overshoot and ringing effect in the DC bus voltage is lessened by the controller action. When there is excess power in the DC bus, the ESS absorbs the surplus power and when there is deficit of power, the ESS provides the deficit power. The transient component of power are provided by supercapacitor. When the battery discharges to its lower limit, load shedding is implemented. When battery charges to its upper SoC limit, the PV and wind system is operated in off-MPPT condition by using droop control.

# CHAPTER 6

## CONCLUSION AND FUTURE SCOPE

### 6.1 Conclusion

The thesis proposes the control strategies in detail for a PV and a PMSG based wind system with hybrid energy storage in a standalone DC microgrid.

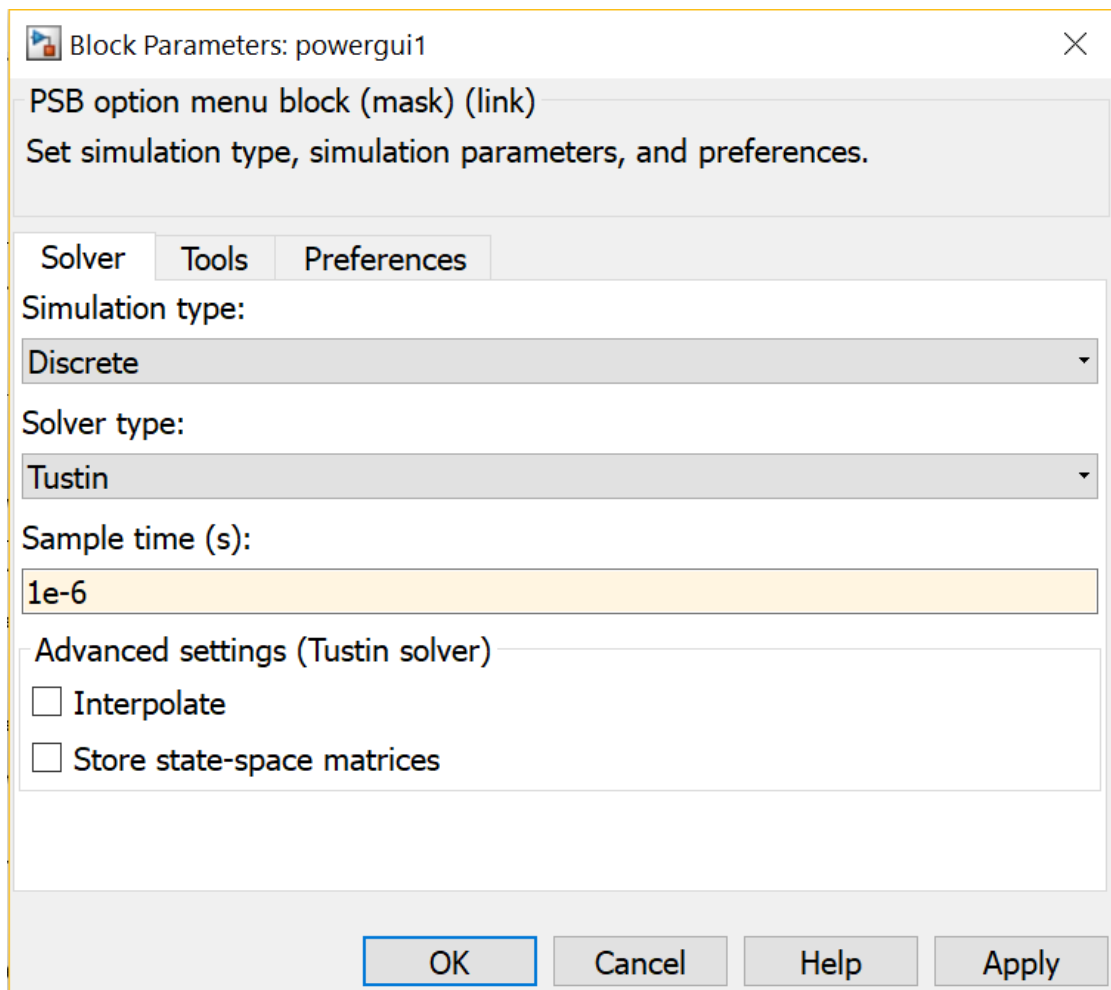
- A power management control algorithm is developed and the system performance is tested under various conditions such as sudden change in load, change in solar irradiance and wind speed, reduced power mode and load shedding.
- The controllers for battery and supercapacitor, designed by frequency domain analysis are also discussed.
- The efficacy of the algorithm is verified with the simulation results.
- The variation of pitch angle during high wind speed to limit the power has also been analysed.
- The results show that the DC link voltage remains constant, under different operating conditions indicating the effectiveness of the proposed strategy.

### 6.2 Future Scope

The experimental validation of the simulation could be done so that the results obtained can be confirmed. The MPPT algorithms for PV and wind system can be modified for better accuracy and fast tracking. The power management algorithm can be extended to grid connected mode so that extra power can be injected into the grid. The stability analysis of the control scheme can be done for determining the operating ranges of load. The control scheme can be extended to multiple PV and wind sources and a robust control algorithm can be formulated by considering different operating conditions. The work can be extended by considering multiple standalone systems interconnected to their neighbouring systems to operate in a unified manner.

# APPENDIX A

## POWERGUI BLOCK IN SIMULINK



Block Parameters: powergui1

PSB option menu block (mask) (link)

Set simulation type, simulation parameters, and preferences.

Solver Tools Preferences

Simulation type:

Discrete

Solver type:

Tustin

Sample time (s):

1e-6

Advanced settings (Tustin solver)

☐ Interpolate

☐ Store state-space matrices

OK Cancel Help Apply

## REFERENCES

- [1] D. E. Olivares, A. Mehrizi Sani, A. H. Etemadi, C. A. Canizares, R. Iravani, M. Kazerani, A. H. Hajimiragha, O. Gomis Bellmunt, M. Saeedifard, R. Palma Behnke, G. A. Jimenez Estevez, and N. D. Hatziargyriou, "Trends in microgrid control," *IEEE Transactions on Smart Grid*, vol. 5, no. 4, pp. 1905–1919, July 2014.
- [2] M. S. Ngan and C. W. Tan, "A study of maximum power point tracking algorithms for stand-alone photovoltaic systems," in *2011 IEEE Applied Power Electronics Colloquium (IAPEC), Malaysia*, April 2011, pp. 22–27.
- [3] M. B. Hemanth Kumar, B. Saravanan, P. Sanjeevikumar, and F. Blaabjerg, "Review on control techniques and methodologies for maximum power extraction from wind energy systems," *IET Renewable Power Generation*, vol. 12, no. 14, pp. 1609–1622, 2018.
- [4] A. Lahyani, P. Venet, A. Guermazi, and A. Troudi, "Battery/supercapacitors combination in uninterruptible power supply (ups)," *IEEE Transactions on Power Electronics*, vol. 28, no. 4, pp. 1509–1522, April 2013.
- [5] A. Merabet, K. Tawfique Ahmed, H. Ibrahim, R. Beguenane, and A. M. Y. M. Ghias, "Energy management and control system for laboratory scale microgrid based wind-pv-battery," *IEEE Transactions on Sustainable Energy*, vol. 8, no. 1, pp. 145–154, Jan 2017.
- [6] S. Kotra and M. K. Mishra, "A supervisory power management system for a hybrid microgrid with hess," *IEEE Transactions on Industrial Electronics*, vol. 64, no. 5, pp. 3640–3649, May 2017.
- [7] G. Ensermu and A. Bhattacharya, "Design of decentralized droop control structure of dc microgrid with constant power loads and source disturbances," in *2018 IEEE Innovative Smart Grid Technologies - Asia (ISGT Asia), Singapore*, May 2018, pp. 91–96.



- [8] S. K. Sahoo, A. K. Sinha, and N. K. Kishore, "Control techniques in ac, dc, and hybrid ac and dc microgrid: A review," *IEEE Journal of Emerging and Selected Topics in Power Electronics*, vol. 6, no. 2, pp. 738–759, June 2018.
- [9] B. K. S. Vastav, S. Nema, P. Swarnkar, and D. Rajesh, "Automatic solar tracking system using delta plc," in *2016 International Conference on Electrical Power and Energy Systems (ICEPES), Bhopal, India*, Dec 2016, pp. 16–21.
- [10] M. G. Molina and P. E. Mercado, *Modelling and Control Design of Pitch-Controlled Variable Speed Wind Turbines*, 2011, exported from <https://app.dimensions.ai> on 2019/04/08. [Online]. Available: <https://app.dimensions.ai/details/publication/pub.1004972900andhttps://www.intechopen.com/chapter/pdf-download/14810>
- [11] A. B. Cultura and Z. M. Salameh, "Modeling and simulation of a wind turbine-generator system," in *2011 IEEE Power and Energy Society General Meeting, San Diego, CA, USA*, July 2011, pp. 1–7.
- [12] B. Wu, Y. Lang, N. Zargari, and S. Kouro, *Wind Generators and Modeling*. IEEE, 2011. [Online]. Available: <https://ieeexplore.ieee.org/document/6047691>
- [13] H. Zhou, T. Bhattacharya, D. Tran, T. S. T. Siew, and A. M. Khambadkone, "Composite energy storage system involving battery and ultracapacitor with dynamic energy management in microgrid applications," *IEEE Transactions on Power Electronics*, vol. 26, no. 3, pp. 923–930, March 2011.
- [14] S. K. Kollimalla, M. K. Mishra, and N. L. Narasamma, "Design and analysis of novel control strategy for battery and supercapacitor storage system," *IEEE Transactions on Sustainable Energy*, vol. 5, no. 4, pp. 1137–1144, Oct 2014.
- [15] R. W. Erickson and D. Maksimovic, *Fundamentals of power electronics*. Springer Science & Business Media, 2007.
- [16] J. Zhang, J. Lai, and W. Yu, "Bidirectional dc-dc converter modeling and unified controller with digital implementation," in *2008 Twenty-Third Annual IEEE Applied Power Electronics Conference and Exposition, Austin, TX, USA*, Feb 2008, pp. 1747–1753.

- [17] N. Zhi, H. Zhang, and X. Xiao, “Switching system stability analysis of dc micro-grids with dbs control,” in *2016 IEEE Applied Power Electronics Conference and Exposition (APEC), Long Beach, CA, USA*, March 2016, pp. 3338–3345.
- [18] M. Gholami, S. H. Fathi, J. Milimonfared, and Z. Chen, “Improving power smoothing and performance of pitch angle system for above rated speed range in wind power systems,” *IET Generation, Transmission Distribution*, vol. 13, no. 3, pp. 409–416, 2019.

## **LIST OF PAPERS BASED ON THESIS**

1. Tony Thomas, Mahesh K. Mishra, "Control Strategy for a PV-Wind based Standalone DC Microgrid with Hybrid Energy Storage System," in *2019 IEEE International Conference on Energy, Systems and Information Processing, Chennai, India*, July 2019. (Accepted)